NAVAL POSTGRADUATE SCHOOL
Monterey, California

THESIS

DETERMINING THE CHARACTERISTICS OF REDUCED-DENSITY CHANNELS IN NH3-N2 GAS MIXTURES

by

William A. Goodwin

June 1988

Thesis Advisor J.R. Neighbours

Approved for public release; distribution is unlimited.

Thesis
G57333

DUDLEY KNOX LIBRARY
NAVAL POSTGRADUATE SCHOOL
MONTEREY, CALIFORNIA 93943-5002

REPORT DOCUMENTATION PAGE

1a Report Security Classification: Unclassified		1b Restrictive Markings	
2a Security Classification Authority		3 Distribution Availability of Report: Approved for public release; distribution is unlimited.	
2b Declassification Downgrading Schedule			
4 Performing Organization Report Number(s)		5 Monitoring Organization Report Number(s)	
6a Name of Performing Organization: Naval Postgraduate School	6b Office Symbol (*if applicable*): 33	7a Name of Monitoring Organization: Naval Postgraduate School	
6c Address (*city, state, and ZIP code*): Monterey, CA 93943-5000		7b Address (*city, state, and ZIP code*): Monterey, CA 93943-5000	
8a Name of Funding Sponsoring Organization	8b Office Symbol (*if applicable*)	9 Procurement Instrument Identification Number	
8c Address (*city, state, and ZIP code*)		10 Source of Funding Numbers	
		Program Element No	Project No / Task No / Work Unit Accession No

11 Title (*include security classification*): THE CHARACTERISTICS OF REDUCED-DENSITY CHANNELS IN NH3-N2 GAS MIXTURES

12 Personal Author(s): William A. Goodwin

13a Type of Report	13b Time Covered	14 Date of Report (*year, month, day*)	15 Page Count
Master's Thesis	From To	June 1988	95

16 Supplementary Notation: The views expressed in this thesis are those of the author and do not reflect the official policy or position of the Department of Defense or the U.S. Government.

17 Cosati Codes			18 Subject Terms (*continue on reverse if necessary and identify by block number*)
Field	Group	Subgroup	Reduced-Density Channel, Fringe Data, Inteferogram, Zero Fringe Line, 2cm reference mark, channel depth, channel width

19 Abstract (*continue on reverse if necessary and identify by block number*)

A CO2 laser was used to generate reduced-density channels in various gas mixtures of ammonia and nitrogen. Interferometers were used to record the changing density resulting from the NH3 absorption of the CO2 laser radiation. One method used to determine the characteristics of the channel was based on the assumption that the resulting density profile was Gaussian shaped. The second method used the Abel Integral Transformation, requiring no pre-conditions on the density profile except that it was cylindrically symmetric. While used extensively in plasma spectroscopy, this technique is not generally well known for analyzing interferometric data. The results show that for a fixed laser energy long, shallow reduced-density channels were formed in gas mixtures of low ammonia concentration and short, deep channels were formed in gas mixtures of high ammonia concentration. These results qualitatively agree with an earlier experiment in which gas mixtures of nitrogen and sulfur-hexaflouride were used. Both experiments support the concept of reduced-density channel formation and lay the foundation for future studies of relativistic electron beam propagation for application in the Strategic Defense Initiative.

20 Distribution Availability of Abstract	21 Abstract Security Classification	
☒ unclassified unlimited ☐ same as report ☐ DTIC users	Unclassified	
22a Name of Responsible Individual: J.R. Neighbours	22b Telephone (*include Area code*): (408) 646-2768	22c Office Symbol: 61Nb

DD FORM 1473,84 MAR 83 APR edition may be used until exhausted
All other editions are obsolete

Approved for public release; distribution is unlimited.

The Characteristics of Reduced-Density Channels in NH3-N2 Gas Mixtures

by

William A. Goodwin
Lieutenant Commander, United States Navy
B.S., United States Naval Academy, 1977

Submitted in partial fulfillment of the
requirements for the degree of

MASTER OF SCIENCE IN PHYSICS

from the

NAVAL POSTGRADUATE SCHOOL
June 1988

ABSTRACT

A CO2 laser was used to generate reduced-density channels in various gas mixtures of ammonia and nitrogen. Interferometers were used to record the changing density resulting from the NH3 absorption of the CO2 laser radiation. One method used to determine the characteristics of the channel was based on the assumption that the resulting density profile was Gaussian shaped. The second method used the Abel Integral Transformation, requiring no pre-conditions on the density profile except that it was cylindrically symmetric. While used extensively in plasma spectroscopy, this technique is not generally well known for analyzing interferometric data. The results show that for a fixed laser energy long, shallow reduced-density channels were formed in gas mixtures of low ammonia concentration and short, deep channels were formed in gas mixtures of high ammonia concentration. These results qualitatively agree with an earlier experiment in which gas mixtures of nitrogen and sulfur-hexaflouride were used. Both experiments support the concept of reduced-density channel formation and lay the foundation for future studies of relativistic electron beam propagation for application in the Strategic Defense Initiative.

- NBS
C-51333
C.2

TABLE OF CONTENTS

I. INTRODUCTION 1

II. DESCRIPTION OF THE REDUCED-DENSITY CHANNEL EXPERIMENT 3
A. EQUIPMENT 3
B. INTERFEROMETERS 4
C. INTERFEROGRAMS 4
D. SUMMARY OF EXPERIMENT 6

III. DATA REDUCTION 7
A. PHOTOGRAPHIC ENLARGEMENT 7
B. DIGITIZING PREPARATIONS 8
C. DIGITIZATION 9
D. FRINGE DATA 10
E. SUMMARY 12

IV. GAUSSIAN ANALYSIS 13
A. THEORY 13
1. Square-Channel 13
2. Non-Uniform Channel 16
B. EVALUATING TEST CELL PARAMETERS 18
C. TEST CASE 21
D. APPLICATION TO EXPERIMENTAL DATA 21
E. SUMMARY 22

V. ABEL ANALYSIS 23
A. ABEL INTEGRAL TRANSFORMATION 23
B. APPLYING THE ABEL TRANSFORMATION 24
C. NUMERICAL SOLUTION 26
D. TEST CASE 27
E. APPLICATION TO EXPERIMENTAL DATA 28
F. SUMMARY 28

VI. RESULTS 29
A. GAUSSIAN-ABEL COMPARISON 29
B. ACCURACY OF RESULTS 30
C. ANALYSIS OF RESULTS 30
1. Channel Density 31
2. Channel Width 32
D. COMPARISON WITH SF6 33
E. CONCLUSIONS 33

LIST OF REFERENCES 35

APPENDIX A. TABLES 37

APPENDIX B. FIGURES 53

INITIAL DISTRIBUTION LIST 82

LIST OF TABLES

Table 1. COORDINATES OF ACTUAL DATA AND ENLARGED DATA ... 37
Table 2. KEY VALUES USED IN ABEL AND GAUSSIAN TECHNIQUES .. 37
Table 3. GAUSSIAN RESULTS FOR 5 TORR NH3/595 TORR N2 38
Table 4. GAUSSIAN RESULTS FOR 15 TORR NH3/585 TORR N2 39
Table 5. GAUSSIAN RESULTS FOR 15 TORR NH3/585 TORR N2 40
Table 6. GAUSSIAN RESULTS FOR 50 TORR NH3/550 TORR N2 41
Table 7. GAUSSIAN RESULTS FOR 50 TORR NH3/550 TORR N2 42
Table 8. GAUSSIAN RESULTS FOR 200 TORR NH3/400 TORR N2 42
Table 9. ABEL RESULTS FOR 5 TORR NH3/595 TORR N2 43
Table 10. ABEL RESULTS FOR 15 TORR NH3/585 TORR N2 44
Table 11. ABEL RESULTS FOR 15 TORR NH3/585 TORR N2 45
Table 12. ABEL RESULTS FOR 50 TORR NH3/550 TORR N2 46
Table 13. ABEL RESULTS FOR 50 TORR NH3/550 TORR N2 47
Table 14. ABEL RESULTS FOR 200 TORR NH3/400 TORR N2 48
Table 15. SUMMARY OF TEST CASE RESULTS 48
Table 16. DENSITY PROFILE OF 600 TORR N2 (ABEL) 49
Table 17. SUMMARY OF RESULTS FOR 5 TORR NH3 50
Table 18. SUMMARY OF RESULTS FOR 15 TORR NH3 50
Table 19. SUMMARY OF RESULTS FOR 15 TORR NH3 51
Table 20. SUMMARY OF RESULTS FOR 50 TORR NH3 51
Table 21. SUMMARY OF RESULTS FOR 50 TORR NH3 52
Table 22. SUMMARY OF RESULTS FOR 200 TORR NH3 52

LIST OF FIGURES

Figure 1. Schematic of Reduced-Density Channel Experiment 53
Figure 2. CO2 Laser Beam Pulse Characteristics 54
Figure 3. Typical Interferogram prior to Energizing CO2 laser 55
Figure 4. Typical Interferogram after Energizing CO2 laser 56
Figure 5. Sketch of Fringe Lines with Key Characteristics Annotated 57
Figure 6. Pattern Used to Test the Enlargement Process 58
Figure 7. Sketch of Interferogram Prepared for Digitizing 59
Figure 8. Sketch of Interferogram Annotated to Resolve Geometry 60
Figure 9. Sketch of Interferogram from Square Channel 61
Figure 10. Sketch of Interferogram from Cylindrical Gaussian Channel 62
Figure 11. Sketch Showing Γ of Asymmetric Fringe Line 63
Figure 12. Schematic View of a Cylindrical Plasma Column 64
Figure 13. Cylindrically Symmetric Test Cell Containing NH3-N2 Gas Mixture . . 65
Figure 14. Abel Determined Density Profile of Gaussian Fringe Pattern 66
Figure 15. Comparison of Fringe Data to Gaussian Curve; Best Case. 67
Figure 16. Comparison of Fringe Data to Gaussian Curve; Worst Case. 68
Figure 17. Plot of On-Axis Density (Abel) vs NH3 Concentration for Test Case and Test Case ± 10 Percent. 69
Figure 18. Variation of Channel Density with Laser Energy at 51 cm from Entrance of Test Cell for 5 torr NH3 (top), 15 torr NH3 (bottom). 70
Figure 19. Variation of Channel Density with Laser Energy at 51 cm from Entrance of Test Cell for 50 torr NH3 (bottom), 200 torr (top). 71
Figure 20. Variation of Channel Density with Laser Energy at 112 cm from Entrance of Test Cell for 5 torr NH3 (top), 15 torr NH3 (bottom). 72
Figure 21. Variation of Channel Density with Laser Energy at 112 cm from entrance of Test Cell for 50 torr NH3. 73
Figure 22. Variation of Channel Density with Laser Energy at 221 cm from Entrance of Test Cell for 5 torr NH3 (top), 15 torr NH3 (bottom). 74
Figure 23. Variation of Channel Density with Distance from Test Cell Entrance for 5, 15, 50 and 200 torr NH3. 75
Figure 24. Variation of Channel Width with Distance from the Test Cell Entrance

for 5, 15, 50 and 200 torr NH3. 76
Figure 25. Predicted Channel Density for 50 joule Laser Energy for Concentrations of .8, 1.2 and 2.0 torr SF6. 77
Figure 26. Variation of Channel Density with Distance from the Test Cell Entrance for 0.2, 0.4, 0.8 and 2.0 torr SF6. 78
Figure 27. Predicted Variation of Channel Density with Laser Energy for 0.4 torr SF6 at 50, 165 and 220 cm from the Test Cell Entrance. 79
Figure 28. Variation of Channel Density with Laser Energy for 0.4 torr SF6 at 17 cm from the Test Cell Entrance. 80
Figure 29. Variation of Channel Density with Laser Energy for 0.4 torr SF6 at 165 cm from the Test Cell Entrance. 81

I. INTRODUCTION

The Strategic Defense Initiative (SDI) was conceived with the goal of making nuclear weapons obsolete. One of the many areas being investigated in the pursuit of this goal is the use of intense high energy electron beams [Ref.1]. In the investigation of these beams, it was found that interaction with the atmosphere reduced electron beam propagation. To improve beam propagation, a method was sought to reduce the atmospheric density along the path of the beam. This method, Reduced-Density Channel formation, consisted of using a laser to pre-condition the atmosphere by creating a region of reduced density along the intended path of the electron beam.

Studies of Reduced Density channels were conducted prior to the establishment of the Strategic Defense Initiative [Refs. 2, 3]. These studies led researchers at the Los Alamos National Laboratory to conduct experiments in channel formation. Two groups of experiments were conducted in which variable laser energies of up to 100 joules were incident on target cells containing gas mixtures. One group of experiments used target cells containing mixtures of nitrogen and sulfur-hexaflouride [Refs. 4 through 7]. The second group of experiments which used target cells containing various mixtures of nitrogen and ammonia are discussed here. A schematic of both experiments is shown in Figure 1.

A CO2 laser beam incident on a target cell containing a mixture of NH3 and N2 creates a region of reduced density when the NH3 partially absorbs the laser enegy. The characteristics of the reduced-density channel are determined by analyzing interferograms taken after the laser was fired.

The CO2 laser used in this experiment was tunable and produced laser pulses up to 300 joules. The laser pulses exhibited a time profile shown in Figure 2 and had a guassian spatial profile. Approximately 33 percent of the beam energy passed through the aperture and energized the gas in the cell: that is a maximum of 100 joules was available for channel formation. As the beam traversed a cylinder filled with a gas mixture of NH3 and N2, a region of reduced density along the longitudinal axis was formed. Three interferometers were positioned at different locations along the cylinder (See Figure 1).

Pictures of the interference patterns, interferograms, were taken to record the effect of the laser beam on the gas. These pictures were then digitized and the information used to determine the depth and width of the resulting channel. Two techniques were used to determine the characteristics of the density channel.

The first technique, the Gaussian method, assumed that the density profile resulting from laser absorption had a Gaussian shape. The second technique developed to determine the channel characteristics required the assumption that the density profile was cylindrically symmetric. The Abel integral transformation, a well known plasma diagnostic technique, was adapted for use with interferometric data. This adaptation is believed to be one of the first applications of the Abel transformation to interferometric data.

This thesis details the procedures used to extract reduced-density channel characteristics from interference patterns recorded during the experiment and constitutes a thorough analysis of all the data from the second group of the Los Alamos experiments.

These results, described in Chapter 6, will indicate:

- For a fixed energy level, increasing the concentration of NH3 results in deeper and shorter reduced-density channels.
- For a Gaussian shaped interference pattern, the Gaussian method of analysis provides a quick and accurate means of determining the reduced-density channel characteristics.

These results are supported by the N2-SF6 experimental results and will be used to study the propagation of intense electron beams through the atmosphere.

II. DESCRIPTION OF THE REDUCED-DENSITY CHANNEL EXPERIMENT

A. EQUIPMENT

A schematic of the experiment is shown in Figure 1. A tunable electron beam controlled CO2 laser with an 11x11x100 cm^3 active volume produced pulses of 10.6 μm radiation at energies of up to 300 joules having a 3.3 μs pulse width. Upon leaving the laser, the radiation experienced multiple reflections as it passed through a nitrogen filled cylindrical tube 10 m long. The reflections served to increase the optical path, hence the laser beam traveled approximately 35 m before exiting the tube and entering the test cell. The increased length aided in focusing the beam; the nitrogen in the cylinder prevented the beam from being scattered by particulate matter. Since nitrogen does not absorb 10.6 μm radiation the laser beam approached the apperture without any significant degradation. One-third of the initial laser energy passed through the aperture and was incident upon the gas at the entrance of the target cell. A typical 60 joule pulse entering the target cell had an estimated peak on-axis fluence of 50 Joules per cm^2. Entering the cell with a full width at half maximum of ~10 mm, the beam was aligned so that the peak of its Gaussian profile was along the longitudinal axis of the cylindrical test cell. [Ref. 8: pp. 4-5].

The test cell, a cylinder 36 cm in diameter and 250 cm long, contained a mixture of NH3 and N2. Experiments in the test cell, were conducted on the following mixtures:

- 5 torr NH3 and 595 torr N2
- 15 torr NH3 and 585 torr N2
- 50 torr NH3 and 550 torr N2
- 200 torr NH3 and 400torr N2

The test cell was evacuated before each experiment. Subsequently it was filled to the desired pressure of NH3 and then brought to atmospheric pressure (600 torr for Los Alamos) with pressurized N2.

The NH3 molecules absorb 10.6 μm radiation [Refs. 9, 10 and 11]. As the beam illuminated the cell, the absorbed energy was transferred to the other molecules of the gas mixture through collisions. The adiabatic expansion of these excited molecules produced a reduced density channel which was centered on the longitudinal axis of the test cell.

An in depth description of the adiabatic expansion process is developed in reference 8 pages 5 through 10. Included in that reference are calculations which determine the required absorbed fluence to produce a unform half density channel 2 m in length. While the values obtained therein apply to 600 torr N2, they apply to the mixtures used in this experiment due to the prominence of the N2 contained in each gas mixture. In short the fluences provided by the CO2 laser were sufficient to produce 2 m long channels which were 1 cm wide and had 0.1 times the ambient density.

In order to observe this reduction in density, windows were installed along the walls of the cell. These windows permitted the use of optical interferometers, one of whose beams traversed the test cell. The density profile of the gas mixture at different locations was then determined by analyzing the interference patterns.

B. INTERFEROMETERS

Three interferometers were installed at different positions along the test cell (See Figure 1). These Mach-Zehnder type of interferometers split the He-Ne laser (633nm) into two separate beams. One beam traversed across the path of the CO2 laser beam and the other beam traversed around it. Figure 3 is a photograph of the pattern resulting from interference of both beams prior to the energizing of the CO2 laser and subsequent channel development. This pattern is due to non-alignment of the mirrors used in the interferometer [Ref. 12]. Filling the test cell with the NH3 and N2 mixture and energizing the CO2 laser developed a phase shift between the two beams. This phase shift was due to a decrease in the optical path length of the beam passing across the path of the CO2 laser. Figure 4 is a photograph of the resulting pattern.

Photographs were taken of each interference pattern observed. These photographs, interferograms, were processed in order to determine the density profile. The processing required photographic enlargment, digitizing and numerical analysis. The following section is devoted to describing terms used in analyzing the interferograms.

C. INTERFEROGRAMS

An interferogram is a photographic record of a pattern produced by an interferometer. In this experiment three separate Mach-Zehnder type interferometers were used at different locations to determine the density profile of a test cell containing a gaseous mixture of NH3 and N2. The following characteristics are used to describe the pattern in an interferogram. Figure 5 is a sketch with these terms clearly annotated.

- Top and Bottom of interferogram.
  The edge of the interferogram towards which the peaks of the fringe line are displaced is the top. The bottom of the interferogram is the edge directly opposite the top.

- 2 cm reference mark.
  In order to establish a scale between the interferograms, a 2 centimeter reference mark was devised and located in the field of view of the camera. This device, a periodic 2 cm square-tooth pattern was used for each interferogram. Portions of the device are visible in Figures 3 and 4. In Figure 5 the device is shown at the top of the sketch. The distance from the right-most corner of one tooth, to the right-most corner of the next tooth was 2 cm.

- Fringe line:
  The interference pattern showns in Figures 3 and 4, also sketched in Figure 5, consist of alternating regions of black and white. Although either region could be used to define a fringe line, the black region is more clearly defined visually. Thus throughout this description, a fringe line refers to a line in the black region which is halfway between two white regions. Figure 5 shows a sketch of two typical fringe lines.

- Fringe number
  The fringe number was arbitrarily chosen to be the number of fringe lines from the bottom of the interferogram. In Figure 4, the third fringe is found by starting at the first black region at the bottom of the interferogram. The fringe line in this region is fringe number one. The next black region encountered as one moves from bottom to top is fringe number two. contains fringe number two. The next region contains fringe number three and so on.

- Zero fringe line.
  A local term used to denote a straight line passing from the left-most edge of a fringe line to the right-most end of the same fringe line. This line corresponds to the interference pattern which would be present if there were no fringe displacement (i.e., no absorbing gas in the test cell). Two of these zero fringe lines are annotated in Figure 5.

- Fringe displacement.
  The distance measured in fringe lines above the zero fringe line. It is due to the decreased optical path length created when the gas mixture absorbs 10.6 μm radiation. To determine fringe displacement, one must find the distance between successive zero fringe lines. A ratio of these numbers yields a scale factor from which any distance measured along the vertical can be converted to a fringe value. In Figure 5, fringe number one has zero fringe displacement at the far left and the far right. The peak of this fringe line is approximately 1.25 fringe lines.

- Vertical reference line.
  A vertical reference line was drawn connecting the peaks of the fringe lines. This line was parallel to the vertical faces of the square tooth but was not necessarily perpendicular to the zero fringe line.

D. SUMMARY OF EXPERIMENT

In this chapter the experiment and its recorded results are described. The next step in trying to determine the density profile and subsequently the characteristics of the reduced-density channel, is to interpret the interferograms. This interpretation is conducted in the next chapter.

III. DATA REDUCTION

Photographs of the interference patterns were taken shortly after the CO_2 Laser energized each gas mixture. These interferograms provided a record from which the fringe data, the relationship between fringe displacement and displacement along the zero fringe line, would be obtained and the on-axis density determined. Once the fringe data was obtained the density profile and subsequently the reduced-density channel characteristics could be determined. This chapter describes how the fringe data was extracted from the interferogram and placed into data files. These files will be analyzed later by the Gaussian and Abel techniques to determine the characteristics of the reduced-density channel formed in each gas mixture.

A. PHOTOGRAPHIC ENLARGEMENT

Determining the fringe data required making measurements directly on the interferogram. To facilitate this procedure, each original interferogram, a photograph measuring approximately 3 cm by 3 cm, was enlarged. The enlargement process was accomplished using a specially modified 35 mm camera fitted with a zoom lens. The image observed in the field of view of the camera was converted to an electronic signal and simultaneously passed to a video screen and Tektronix photo-copier. While monitoring the video screen, the focus of the camera was adjusted until a clear image of the 2 cm reference marks and interference pattern filled the video screen. The 'copy' button of the photo-copier was then depressed, resulting in an enlarged photograph of the interferogram. Some interferograms were not capable of being enlarged with the 2 cm reference marks visible. For those interferograms, a scribe was used to mark the reference points on the orignal photograph. The scribe marks enhanced the image of the reference marks and made them visible in the enlarged interferogram.

Each enlarged photograph therefore contained a set of marks which measured 2 cm in the original interferogram. The distance between these marks varied with each interferogram as a result of the focusing adjustments made during the enlargement process. Thus, all distances could be scaled to the common 2 cm reference mark and continuity was maintained between photographs.

Having enlarged each interferogram, the next step in determining the density profile and subsequently the characteristics of the reduced-density channel was to digitize the enlarged photographs. Before digitizing the interferograms, a one-time check of the combined effects of digitizing and enlarging was conducted by comparing an original drawing to an enlarged copy of the same drawing. A line was drawn on a piece of graph paper and eight easily identified points were then digitized (See Figure 6). The drawing was then enlarged, using the process outlined above, and the same eight points on the enlargement were digitized. The original and resulting coordinates are listed in Table 1. A review of this Table illustrates that the maximum difference between the original and the enlarged copy are within .04 cm of each other. The mean difference between the original and the enlarged copy was no greater than .02 cm for both the vertical and horizontal components. It will be shown in chapter 6 that the errors generated by the enlargement process did not significantly effect the results. The next step in determining the density profile was to prepare the interferograms for digitization.

B. DIGITIZING PREPARATIONS

In preparation for digitization, each enlarged interferogram was reviewed and the following items identified by marking on the photograph. Figure 7 is a sketch of an inteferogram prepared for digitizing.

- 2 cm. reference marks.
  The 2 cm reference mark was identified by drawing a line from the lower right corner of the left-most square tooth, R1, to the same corner of the next square tooth, R2.
- Fringe lines to be digitized.
  Two fringe lines per interferogram were chosen to be digitized. These fringe lines were normally picked based on their clarity and proximity to the center of the interferogram. Three fringe lines labelled F1, F2, and F3 are shown in Figure 7.
- Vertical reference line.
  A vertical reference line was drawn connecting the peaks of the fringe lines. This line was parallel to the vertical faces of the square tooth but was not necessarily perpendicular to the zero fringe line.
- Zero fringe lines.
  Zero fringe lines were drawn for many of the fringe lines of each interferogram. These lines provided the basis for determining the fringe displacement and subsequently the on-axis density. Three zero fringe lines have been drawn in Figure 7.

Having prepared each interferogram for digitizing, the next step was translating the photographic information available from the interferogram to a form which would allow numerical processing.

C. DIGITIZATION

Converting the photographic image of the interference pattern into a form which allows mathematical computation is the process of digitizing.

The first step in the process was to establish a rectangular coordinate system for the interferogram. This was accomplished by designating the left-most point on the fringe line as the origin. This point is labelled P(1) in Figure 7. The vertical axis was made parallel to the vertical reference line of the interferogram and the horizontal axis was chosen perpendicular to this. With this reference system established any point on the interferogram could be designated by a vertical and horizontal component. The HP-9111A Graphics Tablet was used to assign numerical values to these components. The numerical values are in digitizing units, where 1 digitizing unit is equal to 0.025 millimeter [Ref. 13]. The Graphics Tablet can be thought of as an electonic grid with its own rectangular reference system and units. The wand used with the Tablet had a spring loaded tip. With the tip in contact with the Tablet and the spring compressed, the position of the wand relative to the reference system of the Graphics Tablet was registered. This information was then passed to the HP-85 computer and stored in a data file.

Securely fastened to the Tablet using adhesive tape, the interferogram was ready to be processed. This consisted of digitizing the following characteristics of the interferogram.

- 2 cm reference mark.
  Digitizing the right-most corner of one square tooth and then the same corner of the next tooth allowed the distance, in digitizing units, to be determined. This distance corresponded to 2 cm on the interferogram. Refer to points labelled R1 and R2 on Figure 7.

- Distance between zero fringe lines.
  Digitizing the intersection of the vertical reference line and a zero fringe line and the vertical reference line with different zero fringe line allowed a scale factor to be determined. The distance between these two digitized points represented the number of digitizing units per fringe. Refer to points R3, R4 and R5 of Figure 7. Having previously determined the number of digitizing units per 2 cm, a value for the number of fringes per cm was determined.

- Fringe line.
  All fringe lines, two per interferogram, were digitized in the same manner. Starting at the left-most point of the fringe line, point P(1) Figure 7, and proceeding towards the right, approximately 35 points per line were digitized. (See fringe line F1 of Figure 7.) The last point digitized was the right-most point of the fringe line, P(N1).

As the points on the interferogram were digitized they were being stored in a data file. Each digitized fringe line, along with the digitized reference points, was recorded in a separate file.

Each file contained enough information to reproduce the fringe line as it had been digitized. In order to regain the relationship between fringe displacement and distance along the zero fringe line, some data manipulation was needed. This manipulation consisted of correcting the digitized fringe line for the angular difference between the zero fringe line and the horizontal reference line. At this point it is important to recall that the fringe value is determined by the distance the fringe line is away from the zero fringe line-not the horizontal reference line. The following outlines the method used in writing a computer program which converted digitized data into fringe data.

D. FRINGE DATA

The fringe displacement as a function of distance along the zero fringe line defines a rectangular coordinate system. In order to obtain this relationship, a coordinate transformation was made. This transformation required aligning the horizontal axis of the digitized coordinate system with the zero fringe line. The process outlined below follows closely the development of a computer program which performed the transformation. To assist in this development, the following terms are defined.

- J is a number assigned to the point digitized. J = 1 for the first point digitized, J = 2 for the second, and so on.
- F is the number of zero fringe lines between the fringe lines digitized for fringe distance calibration. In Figure 7, the number is 1 if R3 and R4 were digitized. F equals 2 if R3 and R5 were digitized.
- V6 is the angle, in radians, between the zero fringe line and the horizontal axis.
- D1 is the distance, in digitizing units, between the 2 cm reference marks.
- D2 is the distance, in digitizing units, between zero fringe lines digitized for a reference.
- N1 is the last point of the fringe line digitized; the right-most point.
- X1 is the horizontal component of a point in digitizing units.
- Y1 is the vertical component of a point in digitizing units.
- A(J,1) is the horizontal component of a digitized point J.
- A(J,2) is the vertical component of a digitized point J.

In Figure 8, one of the many fringe lines of an interferogram has been sketched and annotated to show the geometry of the coordinate transformation. Having identified the

geometric relationships in the interferogram, the next step in generating fringe data was referencing all digitized points to the origin. This referencing was accomplished by subtracting the coordinates of the origin from each point digitized. As shown:

$$X1 = A(J,1) - A(1,1) \tag{3.1}$$

$$Y1 = A(J,2) - A(1,2) \tag{3.2}$$

The next step was to determine the angle between the zero fringe line and the horizontal axis. This was accomplished by using the first and last points of the digitized fringe line. The ratio of the difference of vertical components to horizontal components was the tangent of the desired angle, V6.

$$X6 = A(N1,1) - A(1,1) \tag{3.3}$$

$$Y6 = A(N1,2) - A(1,2) \tag{3.4}$$

$$V6 = ARCTAN\frac{Y6}{X6} \tag{3.5}$$

With this angle determined, the next step was to relate the horizontal value to a value along the zero fringe line. Since the horizontal component was the projection of the zero fringe line onto the horizontal axis, the distance along the zero fringe line, R8, was found by:

$$R8 = \frac{X1}{\cos(V6)} \tag{3.6}$$

Converting this into centimeters yields the horizontal component of the fringe data

$$R8(J) = R8 \times 2 \times D1 \tag{3.7}$$

The final step in determining the fringe data was to find the fringe value of a vertical component. This was done by finding the contribution to the vertical component made by the zero fringe line and subtracting it from the digitized vertical component.

The vertical contribution of the zero fringe line ,Y8, was determined from:

$$Y8 = X1 \tan(V6) \tag{3.8}$$

This value was subtracted from the vertical component of a digitized point and finding its projection along the horizontal axis.

$$D3 = (Y1 - Y8)\cos(V6) \tag{3.9}$$

The fringe value was finally obtained by multiplying D3 by the ratio of fringes to digitizing units.

$$Y5(J) = \frac{F \times D3}{D2} \tag{3.10}$$

Hence the fringe data originally observed on the interferogram was converted into a numeric form, R8(J) , Y5(J) which allowed mathematical processing.

E. SUMMARY

Digitizing the interferogram was necessary to allow mathematical processing by the computer. In the process, determining the relationship between the fringe displacement and the zero fringe line was required. Having accomplished this, determining the density profile and subsequently the characteristics of the reduced-density channel, using the computer was possible. This determination was conducted using two separate techniques which are addressed in the following chapter.

IV. GAUSSIAN ANALYSIS

A Reduced-Density Channel was generated by firing a CO2 laser beam into a test cell filled with a gas mixture of N2 and NH3. Mach-Zehnder type interferometers were positioned at different locations along the test cell and the resulting interference patterns were recorded on photographic film. These records, interferograms, were analyzed using Gaussian Analysis and Abel Inversion techniques. This chapter is devoted to the development of the Gaussian technique and the numerical manipulation required to obtain the characteristics of the reduced-density channel from the digitized data files using the Gaussian technique. The Abel technique is addressed in the next chapter.

A. THEORY

The Gaussian technique used to determine the characteristics of a reduced density channel was originally developed by Czuchlewski for his experiment with a test cell containing N2 slightly doped with SF6 [Ref. 8: pp. 11-14]. This technique will be presented by first considering a uniform square channel and obtaining a relationship between the on-axis density, fringe displacement and full width at half maximum. The square channel case will then be generalized to cover a non-uniform channel. The result will be a relationship similar to the square channel case, but applicable to the interferograms obtained in the reduced-density channel experiments. In this development a link between the Gaussian and Abel techniques will be identified along with key values used in both techniques. These key values are listed in Table 2. Having determined a relationship between the on-axis density, fringe displacement and full width at half minimum for a non-uniform channel, its application to the stored data files will be described. The results of the Gaussian Analysis for each fringe line are presented in Tables 3 through 6.

1. Square-Channel

Consider a hypothetical situation in which one leg of the interferometer is passing through a square channel. This channel and the resulting interference pattern are shown in Figure 9. Designating the width of the channel as Γ, the optical path difference, OPD, between the arms of the interferometer can be related to the index of refraction in the channel and in the reference beam by:

$$OPD = (n_c - n_o) \times \Gamma \qquad (4.1)$$

where

- n_c is the index of refraction in the channel.
- n_o is the index of refraction in the reference arm of the interferometer.

One fringe shift equates to a phase change of 2π. The fringe shift identified in Figure 9, ΔF, is the optical path difference divided by the wavelength, λ. Substituting this in equation 4.1 yields a relationship between fringe shift, ΔF, and channel width, Γ.

$$\Delta F = (n_c - n_o)\frac{\Gamma}{\lambda} \tag{4.2}$$

The index of refraction is related to the mean polarizability, α, of a gas in CGS notation through the Lorenz-Lorentz relation [Ref. 14: p. 87]

$$\alpha = \frac{3}{4\pi N}\frac{n^2 - 1}{n^2 + 2} = \frac{3}{4\pi N}\frac{\varepsilon - 1}{\varepsilon + 2} \tag{4.3}$$

where

- ε is the dielectric constant.
- n is the index of refraction.
- N is the number of molecules per unit volume.
- $\varepsilon = n^2$.

Making use of the approximation that the index of refraction of a gas is nearly unity, equation 4.3 can be reduced to:

$$\alpha = \frac{n^2 - 1}{4\pi N} \tag{4.4}$$

Rearranging equation 4.4 and solving for the index of refraction yields:

$$n = (1 + 4\pi\alpha N)^{1/2} \tag{4.5}$$

Applying the binomial expansion theorem to equation 4.5 and discarding the higher order terms yields:

$$n = 1 + 2\pi\alpha N \tag{4.6}$$

In order to obtain a relationship between the index of refraction and the density, a connection between the mean polarizability, α , and density must be made. The pertinent connection is made through the molar refractivity, A [Ref. 14: p. 88].

$$A = \frac{4}{3} \times \pi \alpha N_a = \frac{RT}{P} \times \frac{(n^2 - 1)}{3} \tag{4.7}$$

where

- R is the ideal gas constant
- T is the temperature in degrees Kelvin
- P is the pressure of the gas
- N_a is Avagadros number.

Solving equation 4.7 for the index of refraction, n, and using only the first order terms of the binomial expansion theorem yields:

$$n = 1 + \frac{3PA}{2RTN_a} \tag{4.8}$$

Recognizing that the density of a gas, ρ , can be expressed as:

$$\rho = \frac{P}{RT} \tag{4.9}$$

and solving equation 4.8 for the index of refraction in terms of density yields:

$$n - 1 = \frac{3A\rho}{2N_a} \tag{4.10}$$

From equations 4.3 and 4.7 one observes that the mean polarizability, α, and the molar refractivity, A, are constants. This is confirmed by Born and Wolf [Ref. 14: p. 88] as they demonstrate that the molar refractivity of air varies less than 2 percent between pressures of 1 and 42 atmospheres. In their development of the Gaussian analysis, Czuchlewski et al., [Ref. 8: p .11], regard the index of refraction as a product of the density, ρ, and a constant. Hence equation 4.10 can be written as:

$$n - 1 = K\rho \tag{4.11}$$

where

$$K = \frac{3A}{2N_a}. \tag{4.12}$$

Substituting equation 4.11 into equation 4.2 yields a relationship between the fringe shift and the density of the gas mixture.

$$\Delta F = \frac{(K_c\rho_c - K_o\rho_o)\Gamma}{\lambda} \tag{4.13}$$

where

- ρ_c is the density of the gas in the channel
- ρ_o is the density of the gas at ambient conditions

Since it has been determined that A, and subsequently K, is constant, equation 4.13 can be written as:

$$\Delta F = \frac{K\Gamma(\rho_c - \rho_o)}{\lambda} \tag{4.14}$$

Defining δ as the ratio of the on-axis density to the density at the channel wall, allows equation 4.14 to be written as:

$$\Delta F = \frac{(\delta - 1)K\Gamma\rho_o}{\lambda} \tag{4.15}$$

Hence equation 4.15 provides a relationship which allows one to determine the ratio of densities in a square channel test cell by measuring the fringe shift and the full width at half maximum.

$$\delta = 1 - \frac{\Delta F\lambda}{K\rho_o\Gamma} \tag{4.16}$$

Having developed equation 4.16 for the case of a square channel, the next step is to generalize the procedure for a channel which is indicative of the interferograms.

2. Non-Uniform Channel

Consider the interferogram sketched in Figure 10. This represents a non-uniform channel in which the channel density and index of refraction are functions of position, (X,Y). The optical path difference at a position along the y axis can be obtained by an integral along the x axis.

$$OPD(Y) = \int_{-L}^{L} [n_c(X,Y) - n_o] dX \tag{4.17}$$

where L is large enough to extend beyond the limits of the channel. Using the definition of fringe shift, Δ F, and replacing the indices of refraction by there equivalence in terms of density yields:

$$\Delta F(Y) = \frac{K\rho_o}{\lambda} \int_{-L}^{L} [\delta(X,Y) - 1] dX \tag{4.18}$$

Therefore the square channel case, when expanded to cover a general non-uniform channel yields an integral relationship between the fringe shift and the ratio of densities.

The method chosen by Czuchlewski to solve the integral [Ref. 8: p. 13] was to pick a density profile which was cylindrically symmetrical. The function chosen, δ (r), was a Gaussian function and its characterisitics were similar to the actual interferograms.

$$\delta(r) = 1 - (1 - \delta_o) \exp\left(\frac{-2.8r^2}{\Gamma^2}\right) \tag{4.19}$$

where

- δ_o is the ratio of on-axis density to ambient density.
- Γ is the full width of the channel at the half minimum density.

In order to solve equation 4.18 the chosen density profile was converted from cylindrical to cartesian coordinates. This conversion allowed equation 4.19 to be written as:

$$\delta(X,Y) = 1 - (1 - \delta_o) \exp\left[\frac{-2.8(X^2 + Y^2)}{\Gamma^2}\right] \tag{4.19a}$$

Upon substituting equation 4.19a for δ (X,Y) in equation 4.18, one obtains the following expression for the fringe shift:

$$\Delta F(Y) = \frac{K\rho_o}{\lambda} (1 - \delta_o) \exp\left(\frac{-2.8Y^2}{\Gamma^2}\right) \int_{-L}^{L} \exp\left(\frac{-2.8X^2}{\Gamma^2}\right) dX \tag{4.20}$$

The integral of equation 4.20 is Gaussian and its solution allows the fringe shift to be obtained from:

$$\Delta F(Y) = \frac{K\rho_o\Gamma}{\lambda}\left[\frac{\pi}{2.8}\right]^{1/2}(1-\delta_o)\exp\left(\frac{-2.8\,Y^2}{\Gamma^2}\right) \tag{4.21}$$

Evaluating equation 4.21 at Y=0 yields an expression for the non-uniform channel density which closely resembles the relation obtained for the square channel.

$$\Delta F(0) = \frac{K\rho_o\Gamma}{\lambda}\left[\frac{\pi}{2.8}\right]^{1/2}(1-\delta_o) \tag{4.22}$$

Since ΔF and Γ are measurable quantities on the interferogram, the ratio of on-axis density to ambient density can be determined from the following:

$$\delta_o = 1 - \frac{\Delta F(0)}{\Gamma}\left[\frac{\lambda}{K\rho_o}\left(\frac{2.8}{\pi}\right)^{1/2}\right] \tag{4.23}$$

Hereafter the δ_o will be referred to as channel density.

B. EVALUATING TEST CELL PARAMETERS

In the previous section of this chapter a relationship for δ_o was obtained in terms of the fringe shift, ΔF , full width at half maximum, Γ, and some test cell parameters, equation 4.23. Before determining the density profile, these parameters were evaluated.

First consider the parameter λ which represents the wavelength of the laser used in the interferometer. This experiment used a HE-NE laser for the interferometer light source which has a wavelength of 633 nm in vacuum. This wavelength changed with each gas mixture used, however it was determined that the change, 1nm, was not significant. Hence the value of λ was fixed at 633nm throughout these calculations.

Next, consider the parameter, ρ_o, this represents the density of the gas in the reference leg of the interferometer. It was assumed that the ambient conditions for each experiment were the same, 300K and 600 torr. From the ideal gas law the ambient density was found to be:

$$\rho_o = \frac{P}{RT} = \frac{600/760}{83.144\times 300} = 3.165\times 10^{-5} moles/cm^3 = 1.906\times 10^{19} molecules/cm^3$$

The third parameter, K , is proportional to the molar refractivity of the gas mixture. (See equation 4.12). The following describes the procedure used to obtain the molar refractivity and subsequently the value of K for each gas mixture.

Born and Wolf state that the molar refractivity of a gas mixture is equal to the weighted average of the molar refractivities of the constituents [Ref. 14: p. 89]. For the NH3-N2 experiment this can be written as

$$A_{NH3-N2} = \frac{N_{NH3}A_{NH3} + N_{N2}A_{N2}}{N_{NH3} + N_{N2}} \tag{4.24}$$

where

- A_{NH3-N2} is the molar refractivity of the gas mixture
- A_{NH3} is the molar refractivity of NH3
- A_{N2} is the molar refractivity of N2
- N_{NH3} is the number of NH3 molecules in the test cell
- N_{N2} is the number of N2 molecules in the test cell

Therefore to obtain K for a particular gas mixture, the molar refractivity of NH3 and N2 must be determined. The molar refractivity, equation 4.7, is a function of the index of refraction and the density.

Consider first molecular nitrogen, N2. In order to determine its molar refractivity, A, the index of refraction at 633 nm was determined. This was accomplished by interpolating between the values given for 546.1 nm, 1.0002998, and 656.3 nm, 1.0002982, at 0° C and 760 torr [Ref. 15]. The value obtained, 1.00029854 was then corrected to 300K and 600 torr using the Biot-Arago law [Ref. 16: p. 533].

$$n_t - 1 = \frac{n_o - 1}{1 + .00367t}\frac{P}{760} \tag{4.25}$$

where

- n_t is the index of refraction of a gas at temperature, t (degrees Centigrade)
- n_o is the index of refraction of a gas at 0° C and 760 torr
- t is the temperature of the gas in degrees centigrade
- P is the ambient pressure in torr.

Having performed the above corrections, the index of refraction for N2 at 300 K and 600 torr was determined to be 1.000214440.

The tabulated value of the index of refraction for NH3 at the wavelength of sodium D light, 589.5 nm, was available from the Smithsonian Tables [Ref. 16: p. 533]. Insufficient information prevented interpolating to obtain the value at 633 nm. Considering the difference to be quite small, the value at 589.5 nm, 1.000376, was used throughout these calculations. This value was then corrected for temperature and pressure using the same procedure outlined previously for N2. The index of refraction at 300K and 600 torr was determined to be 1.0002700.

The next step in determining the molar refractivity was straightforward application of equation 4.7. This yielded a molar refractivity for N2 as 4.517 cm^3 per mole and for NH3 5.688 cm^3 per mole.

Having determined the molar refractivity for N2 and NH3 equation 4.24 was used to determine the molar refractivity of the gas mixtures. These values are listed in Table 2 along with the values of K , which were determined from the previously developed relationship

$$K = \frac{3A}{2N_a} \tag{4.11}$$

As will be shown later, K is the link between the Gaussian and Abel techniques.

Having determined the numerical values of λ, ρ and K, the relationships for density, equations 4.16 and 4.23, can be reduced to the following:

For uniform square channel

$$\delta = 1 - \frac{\Delta F}{\phi \Gamma} \tag{4.26}$$

For non-uniform square channel

$$\delta_o = 1 - \frac{\Delta F(0)}{1.059 \phi \Gamma} \tag{4.27}$$

where $\phi = \frac{K \rho_o}{\lambda}$

Table 2 lists the value of ϕ and other important parameters for each gas mixture used in the experiment.

C. TEST CASE

Thus far in the development of the Gaussian analysis an algebraic expression has been obtained which allows one to determine the ratio of on-axis density to ambient density for a non-uniform channel, equation 4.27. A test case was generated to check the accuracy of this expression prior to applying it to the actual interferograms.

The test case was a hypothetical cell filled with 600 torr N2 at 300K. Equation 4.21 was used to develope a fringe pattern in which Γ was equal to the square root of 2.8 and δ_o chosen to be 0.1. These conditions reduced equation 4.20 to the following:

$$\Delta F(Y) = 5.40 \exp(-Y^2) \tag{4.28}$$

Equation 4.28 was then solved for the value of Y which yielded one-half the maximum fringe shift. Twice this value, 1.67 cm, corresponds to the full width at half maximum. Evaluating equation 4.27 at this value of Γ, yielded a channel density of 0.10. Thus the equations developed provided self-consistent results.

D. APPLICATION TO EXPERIMENTAL DATA

Having determined that the equations developed for a non-uniform channel provided self-consistent results, each fringe line was analyzed. Due to the asymmetry in the actual interferogram, (See Figure 11), three different values of the full width at half maximum were obtained. These different values correspond to

- Γ_1 the value obtained if the right side were the same as the left side.
- Γ_2 the value obtained if the left side were the same as the right side.
- Γ_3 the value obtained when the left and right side values are averaged.

A computer program was developed which determined the value of Γ and the value of ΔF and then computed the value of the channel density. The results of this program are listed in Tables 3 through 8.

E. SUMMARY

The characteristics of the reduced-density channel are determined by the channel density and the full width at half maximum at a particular location along the test cell. These characteristics have been determined from a method of Gaussian analysis developed by Czuchlewski and are listed in Tables 3 through 8. While this method assumes the density profile is Gaussian, it provides a rapid means of determining an approximate density. Recalling equation 4.27

$$\delta_o = 1 - \frac{\Delta F(0)}{1.059\phi\Gamma} \tag{4.27}$$

it is clear that upon measuring the peak fringe shift and the full width at half maximum a rapid determination of the channel density can be made.

In the next chapter the Abel technique will be used to obtain the same reduced-density channel characteristics.

V. ABEL ANALYSIS

In the previous section a method for determining the ratio of on-axis density to ambient density and width of the reduced density channel was developed assuming the density profile had a Gaussian shape. In this section a method will be developed which makes no such assumption concerning the density profile, but requires the profile to be cylindrically symmetric. This technique was originally developed by Neils Heinrik Abel in the early 1800's in his solution of a mechanics problem. In this section the Abel technique will be developed, applied to a test case and then applied to the interferometric data obtained during the reduced density channel experiment involving NH3-N2 gas mixtures. The results of this analysis are listed in Tables 9 through 14 and provide a determination of the density profile which is representative of the interferometric data.

A. ABEL INTEGRAL TRANSFORMATION

In his short life Neils Heinrik Abel made numerous contributions to the field of mathmatics and science. The significance of many of his contributions were not recognized until more than 100 years after his death in the late 1820's. One area of science which has greatly benefitted from his work is the study of plasma spectroscopy.

While attempting to solve a mechanics problem regarding the velocity of an object along an arc [Ref. 17: p. 97], Abel determined that if a given function, H(a), can be related to another function Ψ by

$$H(a) = \int_0^a \frac{d\Psi}{(a-x)^{\mu}} \tag{5.1}$$

then Ψ can be obtained from

$$\Psi = \frac{\sin \mu\pi}{\pi} \int_0^x \frac{H(a)da}{(x-a)^{1-\mu}} \tag{5.2}$$

where $0 \leq \mu \leq 1$. The full development of this result is available in pages 97 through 103 of Reference 17.

As mentioned this integral transformation is widely used in plasma spectroscopy. In that application the emissivity of a plasma source is determined from the intensity measurements. In the development of this emissivity-intensity relationship for use in plasma spectroscopy, Griem [Ref. 18: p. 176] found the intensity of an optically thin plasma contained by a cylindrical column of radius R_o to be

$$I(Y) = 2\int_0^{(R_o^2 - Y^2)^{1/2}} \varepsilon(r)dX = \int_Y^{R_o} \frac{\varepsilon(r)dr}{(r^2 - Y^2)^{1/2}} \tag{5.3}$$

Using Abel's integral transformation the following determination of the emissivity was obtained (See Figure 12)

$$\varepsilon(r) = \frac{-1}{\pi} \int_r^{R_o} \frac{dI(Y)}{dY} (Y^2 - r^2)^{(-1/2)} dY \tag{5.4}$$

where $\frac{dI(Y)}{dY}$ is the derivative of I(Y) with respect to Y. This same method is used throughout plasma physics in order to determine the emissivity of the source (See Refs. 19 and 20 for examples).

Typically the intensity is a measured quantity and not a differentiable function, hence the solution is accomplished by numerical analysis. Numerous methods of solving equation 5.4 numerically have been identified, some of these may be found in references 21 through 25.

Having identified the Abel integral transformation and one of its more widely used forms, the next step was to find an expression between the fringe data and the density which satisfied the relationship expressed in equations 5.1 and 5.2 . Once identified, the Abel transformation was performed and resulted in an expression for the density as an integral function of the fringe shift.

B. APPLYING THE ABEL TRANSFORMATION

In the Gaussian development an integral expression between fringe shift and density was obtained for the case of the non-uniform channel, equation 4.18. Considering the radial symmetry of the gas, defined by

$$r^2 = X^2 + Y^2 \tag{5.5}$$

Equation 4.18 was written as

$$\Delta F(Y) = \frac{K\rho_o}{\lambda} \int_{-L}^{L} [\delta(r) - 1] dX \tag{5.6}$$

Substituting for dX, its equivalent yielded

$$\Delta F(Y) = \frac{2K\rho_o}{\lambda} \int_{r}^{R_o} \frac{[\delta(r) - 1] r dr}{(r^2 - Y^2)^{1/2}} \tag{5.7}$$

Performing the Abel Transformation on equation 5.7 yielded an expression for ratio of the channel density to ambient density

$$\delta(r) - 1 = \frac{-\lambda}{K\rho_o} \int_{r}^{R_o} \frac{d\Delta F(Y)}{dY} (Y^2 - r^2)^{(-1/2)} dY \tag{5.8}$$

where $\frac{d\Delta F(Y)}{dY}$ is the derivative of ΔF with respect to Y. Hence the ratio of the densities, $\delta(r)$, can be determined by solving the right side of equation 5.8. Attempting to solve this analytically for any but the simplest cases is extremely difficult. Consider as an example the Gaussian test case of the previous chapter. Substituting the derivative of the Gaussian fringe pattern into equation 5.8 produces

$$\delta(r) - 1 = \frac{-\lambda}{K\rho_o} \int_{r}^{R_o} \frac{10.8 Y \exp(-Y^2) dY}{(Y^2 - r^2)^{1/2}} \tag{5.9}$$

Thus even for the situation where the fringe data is given as a differentiable function, numerical analysis is required to solve the right side of equation 5.8.

Having determined that the Abel Integral transformation can be applied to the case of the reduced-density channels, the next step is to determine the method used to obtain a numerical solution to equation 5.8.

As mentioned use of the Abel integral transformation in determining the emissivity of a plasma source is well documented. It is believed that this is one of the first uses of this method in determining the density profile from interferometric data. Solution of this expression, like most Abel integrals is best performed by numerical analysis. In this case

an analytic solution is not readily available. In the case of plasma spectroscopy the intensity is a measured quantity, and not a differentiable function. The next section describes the method used to determine the reduced density channel characteristics using a numerical solution to the Abel integral.

C. NUMERICAL SOLUTION

A sketch of the test cell is provided in Figure 13. This slice of the test cell provides the foundation upon which the Abel technique was developed for obtaining the reduced density channel characteristics of the NH3-N2 gas mixtures.

In the development, it was assumed that a radially symmetric density profile existed after the gas was energized by the incident CO2 laser beam. Further it was assumed that the region could be divided into an infinite number of concentric regions in which the index of refraction was constant. To illustrate this Figure 13 is divided into four regions. The index of refraction at all locations in region σ is the same. Likewise the index of refraction for all locations in region γ is the same and so on for regions η and ν. This is not to imply, however that the index of refraction in region σ is the same as in regions γ , η or ν. Having made these assumptions, an expression for the optical path difference along a chord, C_i, was determined in terms of the notation in Figure 13.

$$C_i = 2\{(n_\sigma - 1)(r_1^2 - Y_1^2)^{1/2} + (n_\gamma - 1)[(r_2^2 - Y_1^2)^{1/2} - (r_1^2 - Y_1^2)^{1/2}] + ...\} \tag{5.10}$$

Expanding this as a series of N regions yields the following

$$C_i = 2\sum_{j=i}^{N-1}(n_j - 1)\{(r_{j+1}^2 - r_i^2)^{1/2} - (r_j^2 - r_i^2)^{1/2}\} \tag{5.11}$$

In order to obtain an expression for the index of refraction, the right side of equation 5.11 was manipulated to obtain

$$n_i - 1 = \frac{C_i - \sum_{j=i+1}^{N-1} 2(n_j - 1)\{(r_{j+1}^2 - r_i^2)^{1/2} - (r_j^2 - r_i^2)^{1/2}\}}{2(r_{i+1}^2 - r_i^2)^{1/2}} \tag{5.12}$$

In continuing with the development of the Abel technique, a relation between the index of refraction and density was required. This relationship was identified in the development of the Gaussian technique as equation 4.11.

$$n - 1 = K\rho \tag{4.11}$$

Writing the previous equation in terms of density and substituting the equivalence of optical path difference, OPD = $\Delta F(Y)\,\lambda$, yielded the following

$$\rho_i = \frac{\Delta F(Y_i)\lambda - \sum_{j=i+1}^{N-1} 2(n_j - 1)\{(r_{j+1}^2 - r_i^2)^{1/2} - (r_j^2 - r_i^2)^{1/2}\}}{2K(r_{j+1}^2 - r_i^2)^{1/2}} \tag{5.13}$$

This equation can be solved by starting at the outer edge of the test cell, $X = R_o$,and proceeding towards the center, X = O. Having obtained an expression for ρ_i, the next step was to determine the ratio of gas density in the channel to the ambient density. This ratio was obtained by scaling the density in the channel. Recall that the density along the axis was determined to be less than the density along the walls of the test cell. Defining a scale comparable to that of the Gaussian technique, δ_o was set equal to:

$$\delta_o = 1 - \frac{\rho_c}{\rho_o} \tag{5.14}$$

One can observe that from equation 5.14, the value of δ_o is 1 at the wall of the cylinder, $\rho_c \ll \rho_o$, and decreases at positions close to the center of the channel.

Having determined a relationship for the density in the channel, a computer program was developed which extracted the density profile of the channel from the fringe data. This method was then checked using the Gaussian test case developed for the Gaussian technique. Application of this test case to the Abel technique is described in the next section.

D. TEST CASE

A method of obtaining the density profile of the test cell using the Abel technique was developed in the previous section. This method was checked using the fringe pattern described by equation 4.28 and found to provide reults of δ_o which agreed with test results to within two decimal places; the results of Γ agreed to within 0.07 cm. Table 15 lists the Abel and test results for δ_o and Γ for each gas mixture used. As an example of

the resultant density profile, the Abel determined profile for 600 torr N2 obtained from the fringe pattern described by equation 4.28 is plotted in Figure 14. The values used to generate the plot are provided in Table 16. Having determined the Abel method produced results which agreed with the test cases, the density profile for each fringe line digitized was determined.

E. APPLICATION TO EXPERIMENTAL DATA

After determining that the Abel technique produced satisfactory results, each fringe line was analyzed to determine the density profile. In doing so it became clear that the slanted interferogram, characteristic of the NH3-N2 gas mixtures, presented a problem that was not encountered with the test case.

In the test case, the fringe lines were divided into two parts and the density profile of each part matched at the origin. In the case of the actual interferograms the difference in fringe patterns on either side of the division line precluded a match at the origin. This difference is consistent with the development of the Abel technique, however it violates the assumption that the density profiles were cylindrically symmetric. At this point the assumption was made that each part of the fringe line represented half of a symmetric fringe line. The value of δ_o to be used in the analysis of the results was an average of the values obtained for both parts of the fringe line. The same procedure was used for determining the value of Γ. The results of Abel analysis on each fringe line are listed in Tables 9 through 14. The values of δ_o are provided for both sides of the division line as well as the average between the two sides. These three values can then be thought as defining the minimum, maximum and most likely value of the on-axis density and channel width.

F. SUMMARY

The Abel technique provided a means to determine the density profile of a gas mixture heated by a CO2 laser beam. From this density profile a determination of the reduced density channel characteristics was possible. In the next chapter results of the the Gaussian and Abel techniques will be used to determine relationships between the channel characteristics and the variables of the experiment, energy and NH3 pressure.

VI. RESULTS

Interferograms made shortly after a CO2 laser energized a test cell containing various mixtures of N2 and NH3 have been analyzed using two different methods. These methods, Gaussian and Abel, have been described in detail in the preceding chapters. In this section a comparison of the two methods and some general observations will be made concerning channel formation.

A. GAUSSIAN-ABEL COMPARISON

A summary of the experimental results is provided in Tables 17-22. Included in these tables is a comparison between the Gaussian and Abel determined values. The closest agreement between the two methods can be found in Table 19. In that Table the results of the experiment for a test cell containing a gas mixture of 15 torr NH3 are listed. At 112 cm along the test cell and for a laser energy of 84 joules, the Gaussian and Abel determined values of δ_o differ by 1.7 percent. Under the same conditions the values determined for Γ differ by 3.6 percent. This fringe pattern and the Gaussian curve obtained by using values of ΔF and Γ obtained from the fringe data are plotted in Figure 15. As expected the two methods yield similar results when the fringe pattern has a Gaussian shape.

In some cases, however, the fringe data are not Gaussian shaped and the analytic analysis is not expected to be very accurate. Consider the results of 5 torr NH3 listed in Table 17. At 51 cm and for an energy of 31 joules, the values of δ_o and Γ obtained by the Gaussian and Abel methods differ appreciably. For δ_o the two analysis methods yield results which differ by 21.1 percent; the values for Γ differ by nearly 331 percent! This fringe line and the corresponding Gaussian curve are plotted in Figure 16. It is apparent from the differences between the curves that the fringe pattern is not Gaussian shaped. Recalling that the Gaussian method uses the maximum fringe shift and the full width at half maximum to determine the value of δ_o and that the Abel method uses all the points digitized along the fringe line, it is easily understood why the two methods yield different results for non-Gaussian shaped fringe patterns.

In general it can be stated that the smaller the difference between the Gaussian and Abel determined values of δ_o and Γ the more nearly the fringe line approximates a Gaussian shape. A review of Tables 17-22 reveals that the Gaussian determined Γ and the Abel determined Γ differ by more than 20 percent in all but 8 of the fringe lines.

The corresponding values of δ_o in these instances differed by less than 5.3 percent. Hence less than 20 percent of the experimental data was Gaussian shaped. For this reason analysis of the reduced-density channel formation will be based on the results obtained from Abel method.

The Gaussian method was developed to provide a quick assessment of the channel formation. From these experimental results it can be stated that for fringe patterns of Gaussian shape, it yielded results very similar to those obtained from the Abel method. For non-Gaussian shaped fringe patterns, it can be stated that it yields values of δ_o within 31 percent of the Abel method. As for the values of Γ obtained, the Gaussian method provided results which were always greater than or equal to the Abel results. Hence, for this experiment the Gaussian method identifies the largest channel width possible.

B. ACCURACY OF RESULTS

In order to provide a determination of the accuracy of the entire process from photographic enlargement through the determination of δ_o, a series of error estimates were made. In these calculations it was assumed that the largest probable error in digitizing a fringe line would be 10 percent of the actual value. Using the fringe pattern described by equation 4.28 two new fringe patterns were generated each differing from the original by 10 percent. One of the fringe patterns generated consistently differed by 10 percent more than the original pattern; the second pattern generated consistently differed by 10 percent less than the original pattern. The results of the Abel determined values of δ_o at each gas mixture are plotted in Figure 17. As can be observed a difference of $\pm$ 10 percent in the fringe pattern results in a $\pm$ 0.09 differnce in δ_o. Since the assumption of 10 percent error incorporates the error introduced in the photographic enlargement process and covers erratic digitizing errors, there is confidence that the values of δ_o are accurate to within $\pm$ 0.09.

C. ANALYSIS OF RESULTS

The Abel method is more dependent on the shape of the entire fringe line than the Gaussian method. To gain insight into the meaning of the results listed in Tables 17-22, several plots of the Abel determined values of δ_o and Γ were made. The results could be plotted in numerous ways, for example δ_o as a function of N13 concentration, laser

energy, distance from the entrance of the cell, etc. The methods chosen to represent the results are δ_o as a function of laser energy, Figures 18-22, and δ_o as function of distance from the test cell entrance, Figures 23 and 24. These two methods will provide a means to compare the results to the results of the SF6 reduced-density channel experiment.

1. **Channel Density**

The following observations were made from the plots of δ_o as a function of energy and with NH3 concentration and distance from cell entrance constant parameters (Figures 18 through 22).

At 51 cm from the entrance of the test cell (See Figures 18 and 19):

- The plots for 5 torr and 200 torr NH3 indicate that there is a slight decrease in δ_o as energy is increased. One could also fit the data with a constant value for δ_o of 0.73 ± 0.05 for 5 torr and 0.83 ± 0.03 for 200 torr. Hence an equally valid interpretation of the results is that there is no apparent energy dependence on the channel depth (Figures 18 and 19).
- For 15 torr (See Figure 18) a pronounced dependence of δ_o on the energy is observed, channel density decreases with increasing energy. At low energies δ_o is observed at values around 0.60, while at higher energies values around 0.30 are observed.
- For 50 torr the channel density decreases with increasing energy through the range of 0 to 43 joules. At 43 joules there appears to be a minimum value and then the channel density begins to increase. This minimum will later be compared to the minimum predicted by the computer model for the SF6 experiment.

At 112 cm from the entrance to the test cell (See Figures 20 and 21):

- For 5 torr there appears to be little effect on δ_o when energy is increased. The results could be fitted with a constant δ_o of 0.73 ± 0.07 (Figure 20).
- For 15 torr a distinguishable dependence of δ_o is observed, channel density decreases as energy increases (Figure 20).
- For 50 torr one can observe remnants of the minimum identified at 51 cm (Figure 21).

At 221 cm from the entrance to the test cell (See Figure 22):

- For 5 and 15 torr NH3 a slight decrease in channel density is observed with increasing energy.
- For 50 and 200 torr NH3 all the laser energy is absorbed at the beginning of the cell and thus, there are no channels at 221 cm.

The results obtained for δ_o are consistent and viable. The following identify traits supporting this

- Plots of δ_o versus energy (Figures 18 through 22) yield smooth curves; there are no discontinuities.

- The values obtained for δ_o under similar conditions yield similar results. An example is the results obtained for 15 torr at 51 cm and 84 joules (Figure 18). The values of δ_o are close and are within the statistical error bar.

To provide further comparisons, representative data points were selected and plotted as a function of position along the test cell in Figures 23 and 24. The energies were selected to provide a means of comparison between different concentrations of NH3. Among the more prominent features of each plot in Figure 23 are

- As the distance from the entrance of the test cell is increased the value of δ_o increases. This finding agrees intuitively with the idea that the laser beam is continuously absorbed as it travels further from the entrance. Hence, there is less energy available at the end of the channel than at the beginning and we expect weaker channels at the end of the cell. The situation for 5 torr, 45 joules and at distances less than 130 cm from the entrance of the cell may be more complicated.
- As the concentration of NH3 increases, the length of the channel decreases. This is evidenced by the fact that no channels exist in 200 torr at 112 cm and none exist at 221 cm for 50 torr. It also agrees intuitively with the idea that as the number of absorbers per unit volume increases, the distance a beam travels before dissipating decreases.
- As the concentration of NH3 increases from 5 to 15 torr, channel density decreases.This is true for all energies plotted and is consistent with the findings of the N2-SF6 experiment. In short, the higher the concentration, the deeper the density channel (Figure 26).
- For a laser energy of 45 joules the channel produced in 5 torr NH3 is relatively constant over the range of 50 to 221 cm with a value of δ_o of 0.79 ± 0.05. This is also true for 75 joules, for which δ_o remains 0.68 ± 0.04. This is similar to the results obtained for the lowest concentration of SF6 [Ref. 8: p. 27], for which relatively long shallow channels were observed.

2. Channel Width

The channel widths for each concentration at selected energies are plotted in Figure 24. The selected energies are the same used in Figure 23 and allow a a comparison between values at the same energy. Unlike the plots of δ_o versus distances, very little consistent information can be garnered from Figure 24. One identifiable characteristic can be observed by considering the 5 and 15 torr concentrations at 51 cm and 112 cm. In these instances the channel width increases as energy increases. The opposite appears true for 200 torr NH3, Γ decreases as energy increases.

D. COMPARISON WITH SF6

At present there is no quantitative method for comparing the characteristics of the reduced-density channel obtained in the NH3-N2 experiment. For that reason the results will be compared with the results of the N2-SF6 reduced-density channel experiment [Ref. 8: p. 27].

The results of the N2-SF6 and the N2-NH3 experiments were very similar. The major differences being that NH3 was substituted for SF6 in the test cell as the 10.6 μm radiation absorber and the measurements were taken at different distances. A computer model, CHANL, developed by Naval Research Laboratory scientists was used to predict the results of the N2-SF6 experiment [Ref. 8: p. 8]. A signficant product of that model is plotted in Figure 25. This figure shows the predicted channel density for a laser energy of 50 joules as a function of distance from the entrance of the test cell. The N2-SF6 experimental results, shown in Figure 26, correlate well with the results of the model. A trend of increasing absorber concentration resulting in shorter, deeper channels is apparent in both plots. When comparing Figures 25 and 26 with the N2-NH3 results shown in Figure 23, the same pattern clearly exists for 5, 15 and 50 torr NH3. Less obvious is the correlation with 200 torr NH3. While only two data points are available, one can assume that the laser energy has been almost totally absorbed before it reached 51 cm. This assumption is supported by Figures 26 and 27.

Figure 27 is another product of the CHANL code. This plot shows the effect on δ_o at 0.4 torr SF6 as energy is increased. Significant is the minimum δ_o which occurs at 50 joules and the sharp change in slope at 165 cm. Evidence of these changes in slope are evident in both the N2-SF6 (Figures 28 and 29) and N2-NH3 (Figures 19 and 21) experimental results.

Based on the above observations, it can be concluded that the N2-NH3 results exhibit the same qualitative behavior as the N2-SF6 results and the CHANL code predictions.

E. CONCLUSIONS

The CO2 laser beam created reduced-density channels in test cells containing a gas mixture of N2 and NH3. These channels were analyzed and found to be dependent on many parameters including the concentration of NH3 and the laser energy. As expected it was found that the depth of the channel decreased as the the beam travelled along the test cell. It was also determined that for a fixed laser energy, the depth of the channel and its length varied inversely with the concentration of NH3. That is, shorter, and

deeper channels were observed at higher concentrations of NH3; long, shallow channels were observed at lower concentrations. This qualitatively agrees with the experimental results and computer predictions for the N2-SF6 experiment [Ref. 8: p. 27].

It can also be concluded that the Gaussian method of analysis provides a quick means of determining the characteristics of a reduced-density channel. The accuracy of the method is dependent upon the shape of the fringe pattern. For Gaussian shaped patterns the results are highly accurate. For non-Gaussian shapes values for δ_o differed from the more accurate Abel method by as much as 31 percent. The channel width determined differed by as much as 330 percent. Despite these large differences the Gaussian method provided a quick means of determining δ_o to within .15 and finding the maximum value of channel width.

To summarize, the analysis of reduced-density channels in gas mixtures of N2 and NH3 support the N2 and SF6 experimental results. The channels obtained in both experiments should be suitable for studying the propagation of intense electron beams through the atmosphere, and thus provides a foundation for determining the role these beams will have in the Strategic Defense Initiative.

LIST OF REFERENCES

1. Hecht J., Beam Weapons, The Next Arms Race, Plenum Press, 1984

2. Askar'yan, G.A. and Tarasova, N.M., Passage of Accelerated Particles and Quanta through a Medium Along an RDC Produced by a Laser Beam, JETP Lett. 20, 123-124, 1974.

3. Masamitsu, J., YU, S. and Chambers, F., Beam Tracking Studies with Ringbearer-II, LLNL Report No. UCID-19771, 1982.

4. Czuchlewski, S.J., Kauppila, T.J., Stout, L.E. and Mitrovich D., Electron-Beam Propagation in a Reduced-Density Channel, Los Alamos National Laboratory Internal Report LA-UR-87-748, March 1987.

5. Mack, J.M. and Czuchlewski, S.J., Theoretical Characterization of Laser-Generated Reduced-Density Channels, Los Alamos National Laboratory Internal Report LA-UR-87-322, September 1987.

6. Czuchlewski, S.J., Carlson, R.L., Kauppila, T.J., Moir, D.C. and Pogue, E.W., Electron Beam Propagation in Laser-Initiated Reduced-Density Channels, Los Alamos National Laboratory Internal Report LA-CP-86-163, 1986.

7. Czuchlewski, S.J., Carlson, R.L., Mack, J.M. and Stout, L.E., Reduced-Density Channels for Electron Beam Propagation, Los Alamos National Laboratory Internal Report LA-CP-85-153, June 1985.

8. Czuchlewski, S.J. and Mack, J.M., "Reduced-Density Channels Generated with a CO2 Laser", Los Alamos National Laboratory, To be published.

9. Murphy, D.P., Raleigh, M., Laikin, E., Peechacek, R.E. and Greig, J.R., REB Channel Tracking Experiments in Low Pressure Ammonia, Naval Research Laboratory Memorandum Report 5281, March 26 1984.

10. Olsen, J.N., "Laser-Initiated Channels for Ion Transport: CO2-Laser Absorption and Heating of NH3 and C2H4 Gases", Journal of Applied Physics, 52 (5), May 1981.

11. Olsen, J.N. and Baker, L., "Laser-Initiated Channels for Ion Transport: Breakdown and Channel Evolution", Journal of Applied Physics, 52 (5), May 1981.

12. Hecht, E. and Sajac, A., Optics, 4th ed., Addison-Wesley Publishing Company Inc., 1979.

13. HP-9111A Graphics Tablet Programming Manual, Hewlett-Packard Company, 1982.

14. Born, M. and Wolf, E., Principles of Optics, 5th. ed., Pergamon Press, 1975.

15. Mellor, J.W., A Comprehensive Treatise on Inorganic and Theoretical Chemistry, Vol. III, Longmans, Green & Co., 1947.

16. Smithsonian Physical Tables, 9th. ed., v 120, Smithsonian Institute, 1954.

17. Sylow, L. and Lie, S. Oeuvres Completes de Niels Heinrik Abel, Grondahl & Son, 1881.

18. Griem, H.R., Plasma Spectroscopy, McGraw-Hill Book Company Inc., 1964.

19. Huddlestone, R.H. and Leonard, S.L., Plasma Diagnostic Techniques, Academic Press, 1965.

20. Harihan, P., Optical Interferometry, Academic Press, 1985.

21. National Aeronautics and Space Administration Technical Note D-5677, A Polynomial Method of Determining Local Emission Intensity by Abel Inversion, by C. Park and D. Moore, February 1970.

22. Vicharelli, P.A. and Lapatovich, W.P., "Iterative Method for Computing the Inverse Abel Transform", Appl. Physics Letter 50 (10), 9 March 1987.

23. Bockasten, K., "Transformation of Observed Radiances into Radial Distribution of the Emission of a Plasma", Journal of Optical Society of America, vol. 51 Nr. 9, September 1961.

24. Barr, W.L., "Method for Computing the Radial Distribution of Emitters in a Cylindrical Source", Journal of Optical Society of America, vol. 52, Nr. 8, August 1962.

25. Nestor, O.H. and Olsen, H.N., "Numerical Methods for Reducing Line and Surface Probe Data", SIAM Review, vol. 2, Nr. 3, July 1960.

APPENDIX A. TABLES

Table 1. COORDINATES OF ACTUAL DATA AND ENLARGED DATA

Point	Original Coordinates		Enlarged Coordinates	
	X	Y	X	Y
A	-.02	.00	-.01	.02
B	1.00	.99	.99	1.03
C	1.98	2.02	1.96	2.02
D	2.98	3.03	2.98	3.01
E	4.03	4.00	4.00	4.00
F	5.03	5.00	5.02	5.01
G	6.04	6.00	6.02	6.01
H	7.06	6.98	7.03	7.01

Table 2. KEY VALUES USED IN ABEL AND GAUSSIAN TECHNIQUES

Pressure (torr)		Density (x E18 molecules per cubic cm)		Molar Refractivity (cubic cm per mole)	K (x E-23 cubic cm per molecule)	$\phi(cm^{-1})$
NH3	N2	NH3	N2			
0	600	0.00	19.06	4.517	1.1247	3.387
5	595	.1583	18.84	4.526	1.127	3.394
15	585	4.75	18.53	4.546	1.132	3.409
50	550	15.83	17.42	4.614	1.149	3.461
200	400	6.33	12.67	4.906	1.222	3.679

Table 3. GAUSSIAN RESULTS FOR 5 TORR NH3/595 TORR N2

DATA FILE	FRINGE	DIST FROM SOURCE (cm)	ENERGY (joules)	GAUSSIAN ANALYSIS (ON-AXIS DENSITY)			
				Full	Left	Right	Ave
Test	1	NA	NA	.105	.105	.105	.105
966A4	4	51	31	.860	.712	.910	.827
966A5	5	51	31	.866	.717	.912	.832
966B4	4	112	31	.851	.867	.825	.848
966B5	5	112	31	.850	.877	.809	.845
964A7	7	51	75	.661	.714	.584	.653
964A6	6	51	75	.692	.755	.587	.678
964B3	3	112	75	.746	.794	.670	.737
964B2	2	112	75	.724	.788	.607	.706
964C1	1	221	75	.821	.818	.824	.821
963A4	4	51	45	.805	.856	.697	.786
963A5	5	51	45	.834	.880	.728	.814
963B2	2	112	45	.765	.820	.662	.749
963B3	3	112	45	.814	.866	.693	.791
963C2	2	221	45	.882	.841	.906	.876
962A4	4	51	57	.834	.885	.696	.805
962A5	5	51	57	.770	.828	.654	.750
962B2	2	112	57	.800	.838	.739	.792
962B5	5	112	57	.842	.893	.695	.810
962C1	1	221	57	.900	.911	.884	.898

Table 4. GAUSSIAN RESULTS FOR 15 TORR NH3/585 TORR N2

DATA FILE	FRINGE	DIST FROM SOURCE (cm)	ENERGY (joules)	GAUSSIAN ANALYSIS (ON-AXIS DENSITY)			
				Full	Left	Right	Ave
Test	1	NA	NA	.109	.109	.109	.109
960A6	6	51	36	.620	.683	.529	.609
960A5	5	51	36	.619	.673	.543	.612
960B2	2	112	36	.703	.747	.639	.696
960B5	5	112	36	.735	.783	.660	.726
960C2	2	221	36	.912	.905	.918	.911
959A7	7	51	46	.622	.685	.529	.612
959A6	6	51	46	.648	.718	.534	.633
959B1	1	112	46	.674	.733	.580	.662
959B2	2	112	46	.698	.716	.678	.698
959C2	2	221	46	.888	.904	.866	.886
958A4	4	51	84	.313	.229	.381	.308
958A6	6	51	84	.414	.312	.490	.405
958B3	3	112	84	.537	.614	.426	.527
958B4	4	112	84	.976	.980	.971	.976

Table 5. GAUSSIAN RESULTS FOR 15 TORR NH3/585 TORR N2

DATA FILE	FRINGE	DIST FROM SOURCE (cm)	ENERGY (joules)	GAUSSIAN ANALYSIS (ON-AXIS DENSITY)			
				Full	Left	Right	Ave
Test	1	NA	NA	.109	.109	.109	.109
957A4	4	51	84	.265	.325	.193	.261
957A5	5	51	84	.217	.298	.114	.210
957B4	4	112	84	.588	.629	.537	.576
957B7	7	112	84	.594	.631	.550	.592
956A4	4	51	57	.357	.393	.317	.356
956A6	6	51	57	.361	.395	.323	.360
956B3	3	112	57	.654	.684	.619	.652
956B6	6	112	57	.654	.702	.587	.648
956C2	2	221	57	.835	.793	.863	.830
955A4	4	51	61	.275	.353	.176	.268
955A6	6	51	61	.398	.457	.325	.393
955B2	2	112	61	.647	.674	.616	.646
955B5	5	112	61	.635	.663	.602	.633

Table 6. GAUSSIAN RESULTS FOR 50 TORR NH3/550 TORR N2

DATA FILE	FRINGE	DIST FROM SOURCE (cm)	ENERGY (joules)	GAUSSIAN ANALYSIS (ON-AXIS DENSITY)			
				Full	Left	Right	Ave
Test	1	NA	NA	.124	.124	.124	.124
877B5	5	112	63	.816	.847	.768	.810
877B4	4	112	63	.814	.815	.813	.814
877A6	6	51	63	.484	.513	.452	.483
877A5	5	51	63	.433	.490	.363	.429
878B7	7	112	76	.761	.790	.724	.758
878B8	8	112	76	.769	.795	.737	.767
878A7	7	51	76	.478	.432	.518	.476
878A6	6	51	76	.515	.477	.547	.513
879B6	6	112	72	.797	.777	.813	.796
879B5	5	112	72	.761	.784	.732	.759
879A5	5	51	72	.521	.521	.521	.521
879A4	4	51	72	.554	.570	.537	.554
880B7	7	112	73	.785	.770	.798	.784
880B6	6	112	73	.765	.752	.777	.765

Table 7. GAUSSIAN RESULTS FOR 50 TORR NH3/550 TORR N2

DATA FILE	FRINGE	DIST FROM SOURCE (cm)	ENERGY (joules)	GAUSSIAN ANALYSIS (ON-AXIS DENSITY)			
				Full	Left	Right	Ave
Test	1	NA	NA	.124	.124	.124	.124
973B2	2	112	12	.830	.856	.793	.826
973B1	1	112	12	.854	.898	.740	.830
973A4	4	51	12	.641	.610	.666	.639
973A5	5	51	12	.683	.665	.700	.683
974B5	5	112	39	.780	.882	.713	.772
974B2	2	112	39	.718	.762	.653	.711
974A7	7	51	39	.439	.438	.441	.439
974A6	6	51	39	.417	.414	.419	.417
976B3	3	112	42	.720	.774	.632	.701
976B2	2	112	39	.703	.778	.557	.661
976A5	5	51	42	.439	.352	.506	.422
976A4	4	51	42	.345	.259	.413	.325
977B5	5	112	43	.780	.830	.688	.751
977B4	4	112	43	.739	.797	.635	.716
977A3	3	51	43	.636	.452	.727	.595
977A2	2	51	43	.567	.400	.661	.530

Table 8. GAUSSIAN RESULTS FOR 200 TORR NH3/400 TORR N2

DATA FILE	FRINGE	DIST FROM SOURCE (cm)	ENERGY (joules)	GAUSSIAN ANALYSIS (ON-AXIS DENSITY)			
				Full	Left	Right	Ave
Test	1	NA	NA	.182	.182	.182	.182
874A6	6	51	118	.893	.897	.888	.893
874A5	5	51	118	.882	.858	.899	.880
876A5	5	51	203	.888	.892	.884	.888
876A4	4	51	203	.895	.897	.892	.895

Table 9. ABEL RESULTS FOR 5 TORR NH3/595 TORR N2

DATA FILE	FRINGE	DIST FROM SOURCE (cm)	ENERGY (joules)	ABEL ANALYSIS (ON-AXIS DENSITY)		
				Left	Right	Ave
Test	1	NA	NA	.102	.102	.102
966A4	4	51	31	.662	.733	.697
966A5	5	51	31	.638	.773	.705
966B4	4	112	31	.856	.752	.804
966B5	5	112	31	.889	.724	.806
964A7	7	51	75	.713	.528	.621
964A6	6	51	75	.716	.609	.663
964B3	3	112	75	.759	.581	.670
964B2	2	112	75	.799	.565	.622
964C1	1	221	75	.585	.840	.713
963A4	4	51	45	.741	.716	.728
963A5	5	51	45	.840	.764	.802
963B2	2	112	45	.829	.608	.719
963B3	3	112	45	.806	.639	.723
963C2	2	221	45	.787	.894	.840
962A4	4	51	57	.676	.680	.678
962A5	5	51	57	.731	.591	.661
962B2	2	112	57	.828	.774	.801
962B5	5	112	57	.864	.647	.756
962C1	1	221	57	.874	.860	.867

Table 10. ABEL RESULTS FOR 15 TORR NH3/585 TORR N2

DATA FILE	FRINGE	DIST FROM SOURCE (cm)	ENERGY (joules)	ABEL ANALYSIS (ON-AXIS DENSITY)		
				Left	Right	Ave
Test	1	NA	NA	.106	.106	.106
960A6	6	51	36	.605	.499	.552
960A5	5	51	36	.642	.536	.589
960B2	2	112	36	.684	.590	.637
960B5	5	112	36	.686	.636	.661
960C2	2	221	36	.888	.905	.897
959A7	7	51	46	.720	.493	.607
959A6	6	51	46	.720	.560	.640
959B1	1	112	46	.663	.540	.602
959B2	2	112	46	.687	.716	.702
959C2	2	221	46	.901	.803	.852
958A4	4	51	84	.226	.382	.305
958A6	6	51	84	.387	.310	.348
958B3	3	112	84	.590	.301	.445

Table 11. ABEL RESULTS FOR 15 TORR NH3/585 TORR N2

DATA FILE	FRINGE	DIST FROM SOURCE (cm)	ENERGY (joules)	ABEL ANALYSIS (ON-AXIS DENSITY)		
				Left	Right	Ave
Test	1	NA	NA	.106	.106	.106
957A4	4	51	84	.392	.120	.256
957A5	5	51	84	.330	.051	.190
957B4	4	112	84	.580	.553	.566
957B7	7	112	84	.628	.533	.581
956A4	4	51	57	.419	.256	.337
956A6	6	51	57	.460	.236	.348
956B3	3	112	57	.661	.611	.636
956B6	6	112	57	.687	.483	.585
956C2	2	221	57	.713	.818	.766
955A4	4	51	61	.412	.006	.209
955A6	6	51	61	.396	.232	.314
955B2	2	112	61	.594	.501	.548
955B5	5	112	61	.552	.511	.532

Table 12. ABEL RESULTS FOR 50 TORR NH3/550 TORR N2

DATA FILE	FRINGE	DIST FROM SOURCE (cm)	ENERGY (joules)	ABEL ANALYSIS (ON-AXIS DENSITY)		
				Left	Right	Ave
Test	1	NA	NA	.121	.121	.121
877B5	5	112	63	.867	.780	.823
877B4	4	112	63	.810	.783	.797
877A6	6	51	63	.585	.442	.513
877A5	5	51	63	.432	.352	.392
878B7	7	112	76	.781	.572	.676
878B8	8	112	76	.742	.706	.724
878A7	7	51	76	.438	.561	.499
878A6	6	51	76	.469	.561	.515
879B6	6	112	72	.765	.726	.746
879B5	5	112	72	.793	.743	.768
879A5	5	51	72	.586	.564	.575
879A4	4	51	72	.542	.552	.547
880B7	7	112	73	.738	.725	.732
880B6	6	112	73	.577	.684	.630
880A6	6	51	73	.675	.547	.610

Table 13. ABEL RESULTS FOR 50 TORR NH3/550 TORR N2

DATA FILE	FRINGE	DIST FROM SOURCE (cm)	ENERGY (joules)	ABEL ANALYSIS (ON-AXIS DENSITY)		
				Left	Right	Ave
Test	1	NA	NA	.121	.121	.121
973B2	2	112	12	.788	.679	.733
973B1	1	112	12	.860	.625	.743
973A4	4	51	12	.568	.620	.595
973A5	5	51	12	.666	.721	.694
974B5	5	112	39	.772	.618	.695
974B2	2	112	39	.705	.636	.670
974A7	7	51	39	.438	.335	.387
974A6	6	51	39	.368	.276	.322
976A5	5	51	42	.310	.464	.387
976A4	4	51	42	.036	.317	..177
976B3	3	112	42	.653	.524	.589
976B2	2	112	42	.683	.446	.564
977A3	3	51	43	.372	.549	.411
977A2	2	51	43	.324	.437	.381
977B5	5	112	43	.637	.641	.639
977B4	4	112	43	.656	.572	.614

Table 14. ABEL RESULTS FOR 200 TORR NH3/400 TORR N2

DATA FILE	FRINGE	DIST FROM SOURCE (cm)	ENERGY (joules)	ABEL ANALYSIS (ON-AXIS DENSITY)		
				Left	Right	Ave
Test	1	NA	NA	.179	.179	.179
874A6	6	51	118	.880	.833	.857
874A5	5	51	118	.850	.848	.849
876A5	5	51	203	.820	.800	.810
876A4	4	51	203	.700	.855	.777

Table 15. SUMMARY OF TEST CASE RESULTS

Pressure (torr)		K (x E-23 cubic cm per molecule)	Channel Density (δ_o)		Full Width at Half Min; Γ (cm)	
NH3	N2		Abel	Test	Abel	Test
0	600	1.1247	.102	.100	1.60	1.67
5	595	1.127	.102	.105	1.60	1.67
15	585	1.132	.106	.109	1.60	1.67
50	550	1.149	.121	.124	1.60	1.67
200	400	1.222	.179	.182	1.60	1.67

Table 16. DENSITY PROFILE OF 600 TORR N2 (ABEL)

Left Side		Right Side	
Dist from Origin (cm)	On-Axis Density	Dist from Origin (cm)	On-Axis Density
2.20	1.00	2.20	1.00
1.56	0.95	1.56	0.95
1.30	0.88	1.30	0.88
1.14	0.79	1.14	0.79
1.01	0.70	1.01	0.70
0.89	0.62	0.89	0.62
0.78	0.54	0.78	0.54
0.66	0.47	0.66	0.47
0.55	0.37	0.55	0.37
0.43	0.28	0.43	0.28
0.26	0.22	0.26	0.22
0.00	0.10	0.00	0.10

Table 17. SUMMARY OF RESULTS FOR 5 TORR NH3

Energy (joules)	Dist from Source (cm)	ON-AXIS DENSITY (δ)					Full Width at Half Min (Γ)				
		Abel	±	Gauss	±	Δ%	Abel	±	Gauss	±	Δ%
31	51	.71	.06	.86	0.0	21.1	.36	.03	1.55	.06	330.6
45	51	.77	.05	.82	.02	5.2	.73	.17	1.39	.13	90.4
57	51	.68	.06	.80	.03	17.6	.50	.02	1.48	.26	196.0
75	51	.65	.09	.68	.02	4.6	.79	.05	1.11	.04	40.5
31	112	.81	.08	.85	0.0	4.9	.48	.07	.81	.03	68.8
45	112	.73	.11	.79	.03	8.2	.80	.05	1.17	.24	46.3
57	112	.78	.09	.82	.02	5.1	.88	.17	1.41	.25	60.2
75	112	.69	.12	.74	.01	7.2	.93	.11	1.19	.06	28.0
45	221	.85	.05	.88	.04	3.4	.42	NA	.78	NA	85.7
57	221	.87	.07	.90	.02	3.4	.45	.03	.96	.18	46.8
75	221	.72	.12	.82	.05	13.9	.45	NA	.87	NA	93.3

Table 18. SUMMARY OF RESULTS FOR 15 TORR NH3

Energy (joules)	Dist from Source (cm)	ON-AXIS DENSITY (δ)					Full Width at Half Min (Γ)				
		Abel	±	Gauss	±	Δ%	Abel	±	Gauss	±	Δ%
36	51	.58	.06	.62	.01	6.9	.77	.05	1.14	.03	48.1
46	51	.63	.11	.64	.02	1.6	.79	.02	1.04	.07	31.7
57	51	.36	.11	.36	.01	0.0	.83	.01	.95	.04	14.5
61	51	.28	.18	.34	.09	21.4	.73	.08	.89	.05	21.9
84	51	.32	.08	.36	.07	12.5	.95	.07	1.21	.16	27.4
84	51	.24	.16	.24	.03	0.0	.88	.03	.94	0.0	6.8

Table 19. SUMMARY OF RESULTS FOR 15 TORR NH3

Energy (joules)	Dist from Source (cm)	ON-AXIS DENSITY (δ)					Full Width at Half Min (Γ)				
		Abel	±	Gauss	±	Δ%	Abel	±	Gauss	±	Δ%
36	112	.66	.04	.72	.02	9.1	.70	.07	1.17	0.5	67.1
46	112	.66	.08	.69	.01	4.6	.78	.20	.91	.15	16.7
57	112	.62	.09	.65	0.0	6.5	.92	.11	1.15	.01	25.0
61	112	.55	.04	.64	.01	16.4	.80	.05	1.11	.01	38.8
84	112	.58	.04	.59	0.0	1.7	1.11	.02	1.15	0.0	3.6
36	221	.90	.09	.91	NA	1.1	.72	NA	1.15	NA	59.7
46	221	.85	.01	.89	NA	4.7	.65	NA	.99	NA	52.3
57	221	.77	.05	.84	NA	9.1	.46	NA	.95	NA	106.5

Table 20. SUMMARY OF RESULTS FOR 50 TORR NH3

Energy (joules)	Dist from Source (cm)	ON-AXIS DENSITY (δ)					Full Width at Half Min (Γ)				
		Abel	±	Gauss	±	Δ%	Abel	±	Gauss	±	Δ%
12	51	.65	.06	.66	.03	1.5	.70	.16	.99	.04	41.4
39	51	.37	.07	.43	.02	16.2	.91	.03	1.15	.03	26.4
42	51	.28	.18	.39	.07	28.6	.75	.07	1.49	.14	98.7
43	51	.42	.10	.60	.05	30.2	.93	.16	1.16	.11	24.7
63	51	.46	.10	.46	.04	0.0	.84	.13	.94	0.0	11.9
72	51	.57	.02	.54	.02	5.3	.85	.05	.98	.04	15.3
73	51	.62	.06	.61	NA	1.6	.87	NA	1.22	NA	40.2
76	51	.52	.06	.50	.03	3.8	1.02	.06	1.17	.06	14.7

Table 21. SUMMARY OF RESULTS FOR 50 TORR NH3

Energy (joules)	Dist from Source (cm)	ON-AXIS DENSITY (δ)					Full Width at Half Min (Γ)				
		Abel	±	Gauss	±	Δ%	Abel	±	Gauss	±	Δ%
12	112	.74	.10	.84	.02	13.5	.42	.19	1.12	.04	166.7
39	112	.69	.07	.75	.04	8.1	.83	.11	1.21	.02	45.8
42	112	.58	.11	.71	.01	18.5	.59	.01	1.31	.09	122.0
43	112	.63	.04	.76	.03	17.1	.62	.04	1.08	.15	74.2
63	112	.81	.04	.82	0.0	1.2	1.05	.15	1.26	0.0	20.0
72	112	.76	.03	.78	.03	2.6	.91	.25	1.18	.08	29.7
73	112	.69	.07	.78	.01	13.0	.59	.37	1.22	.04	106.8
76	112	.71	.09	.77	.01	8.5	.63	.13	1.01	.02	60.3

Table 22. SUMMARY OF RESULTS FOR 200 TORR NH3

Energy (joules)	Dist from Source (cm)	ON-AXIS DENSITY (δ)					Full Width at Half Min (Γ)				
		Abel	±	Gauss	±	Δ%	Abel	±	Gauss	±	Δ%
39	51	.85	.02	.89	.01	4.1	.69	0.0	1.52	.05	120.3
68	51	.80	.07	.89	0.0	10.2	.35	.06	1.16	.52	231.4

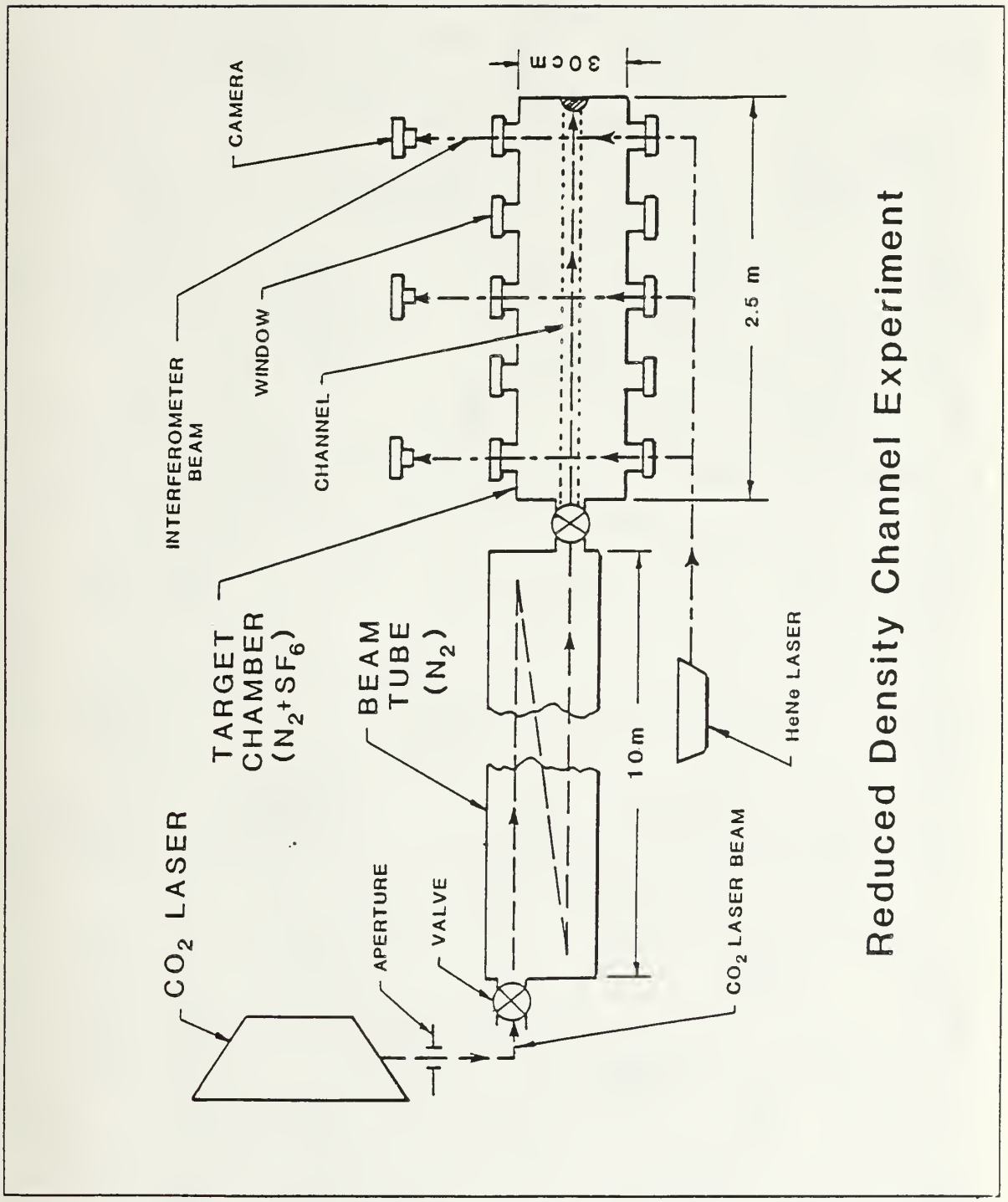

Figure 1. Schematic of Reduced-Density Channel Experiment

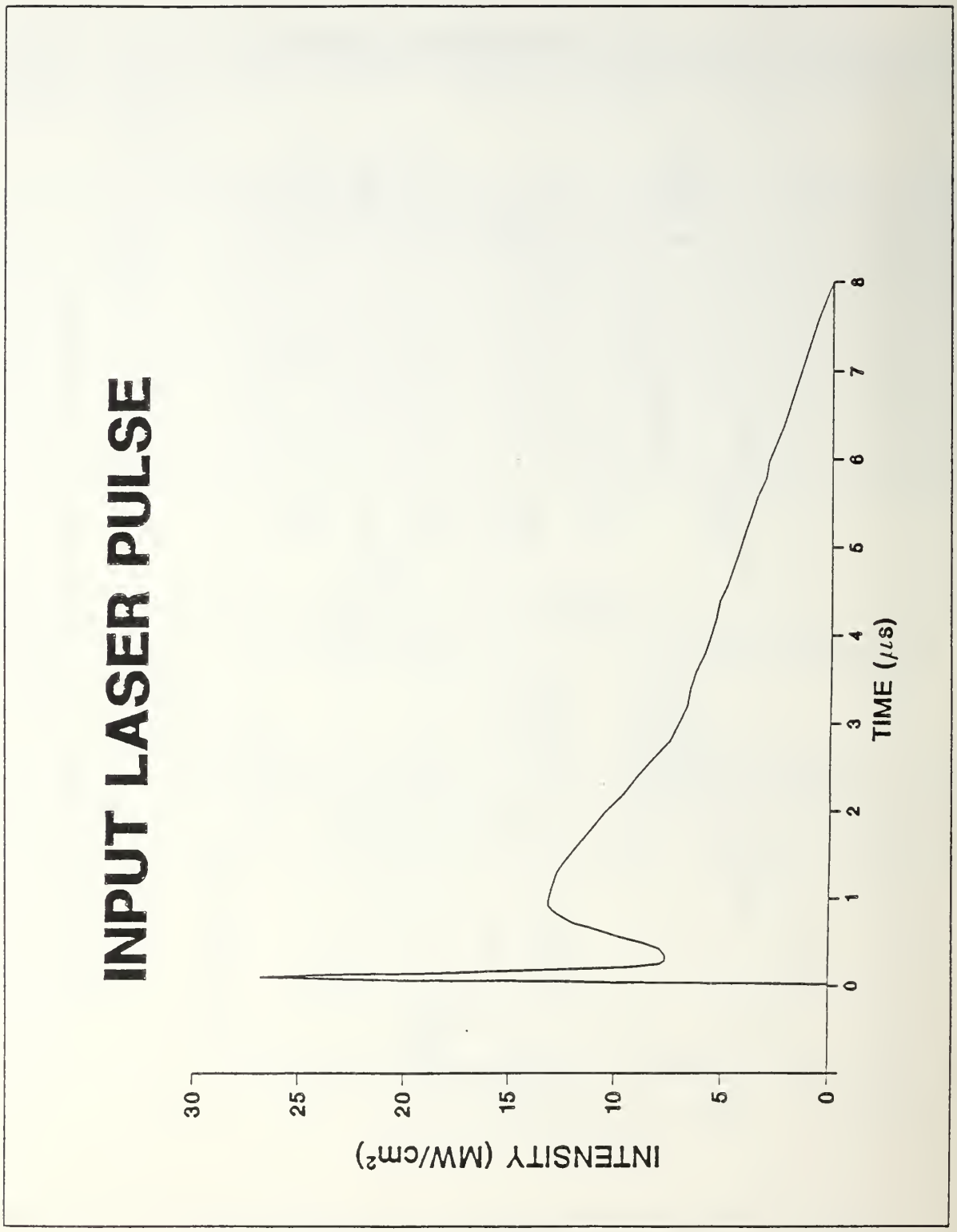

Figure 2. CO2 Laser Beam Pulse Characteristics

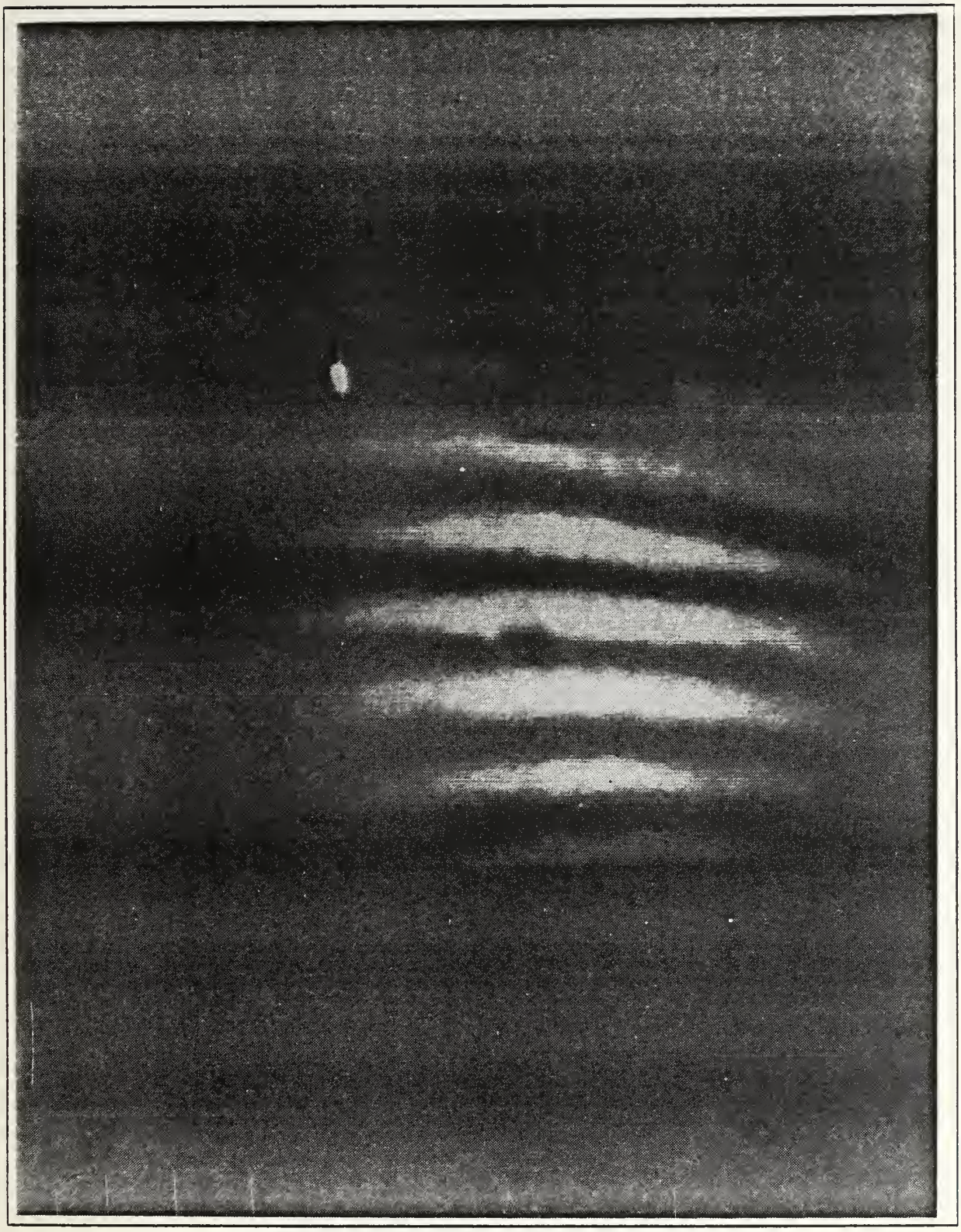

Figure 3. Typical Interferogram prior to Energizing CO2 laser

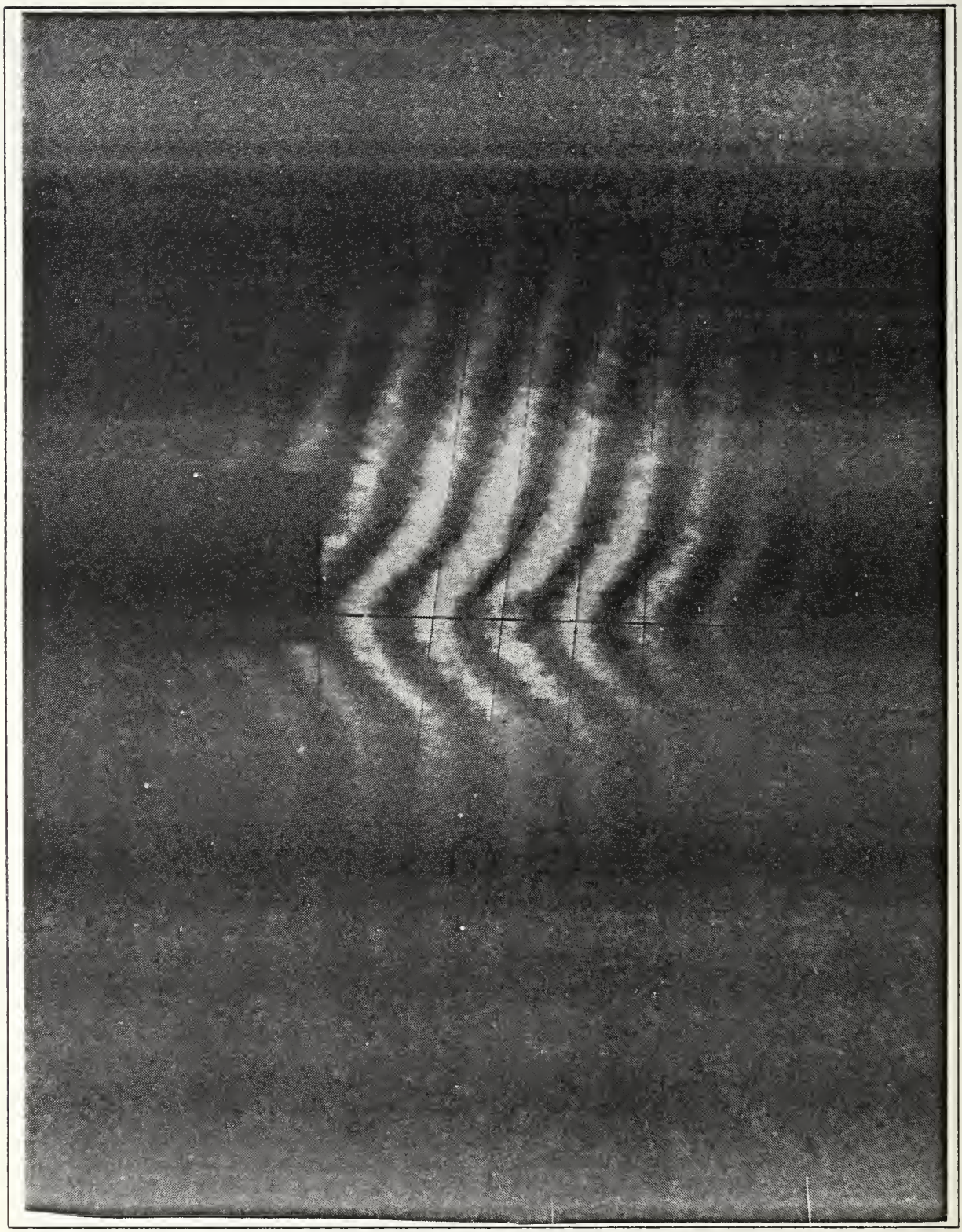

Figure 4. Typical Interferogram after Energizing CO_2 laser

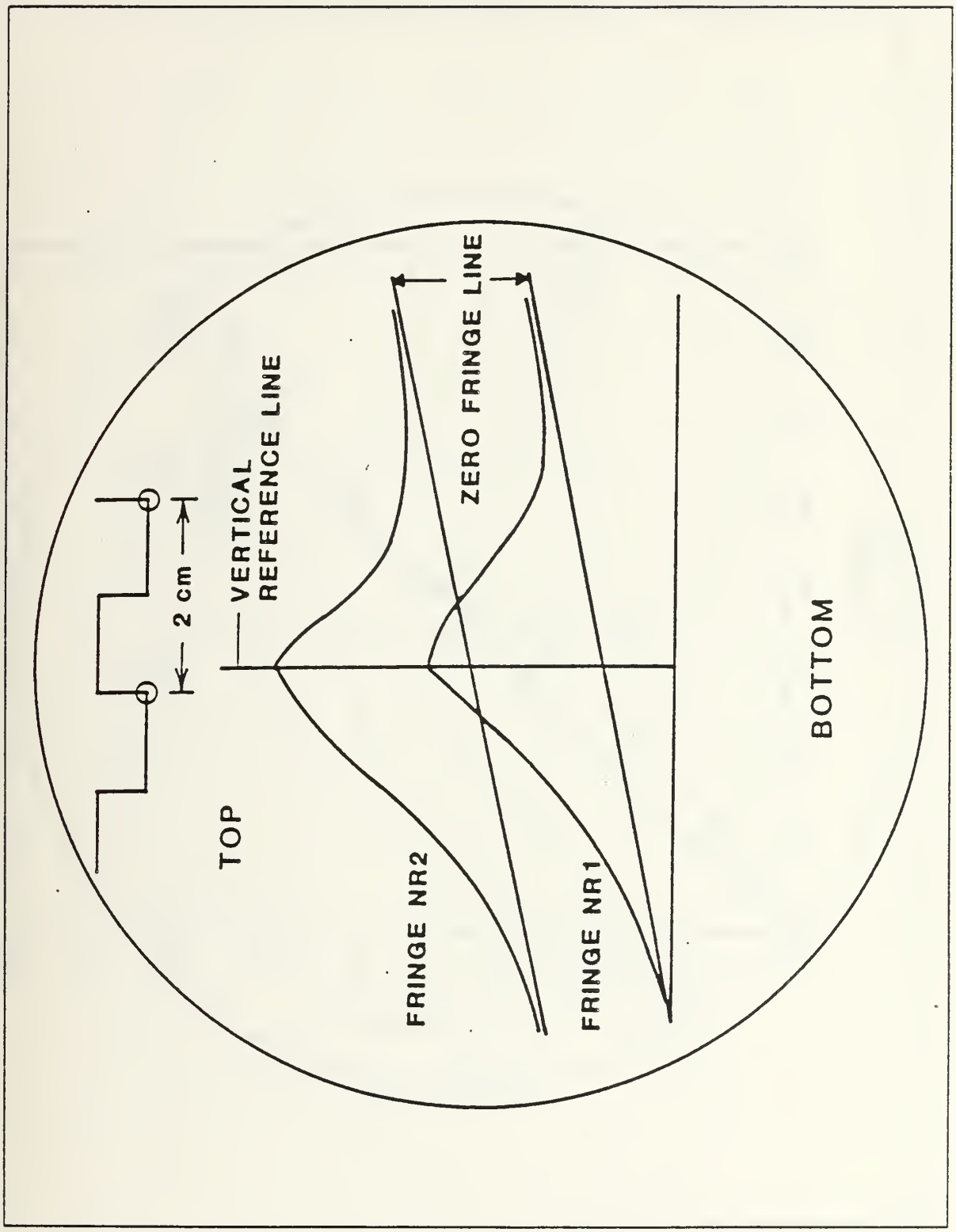

Figure 5. Sketch of Fringe Lines with Key Characteristics Annotated

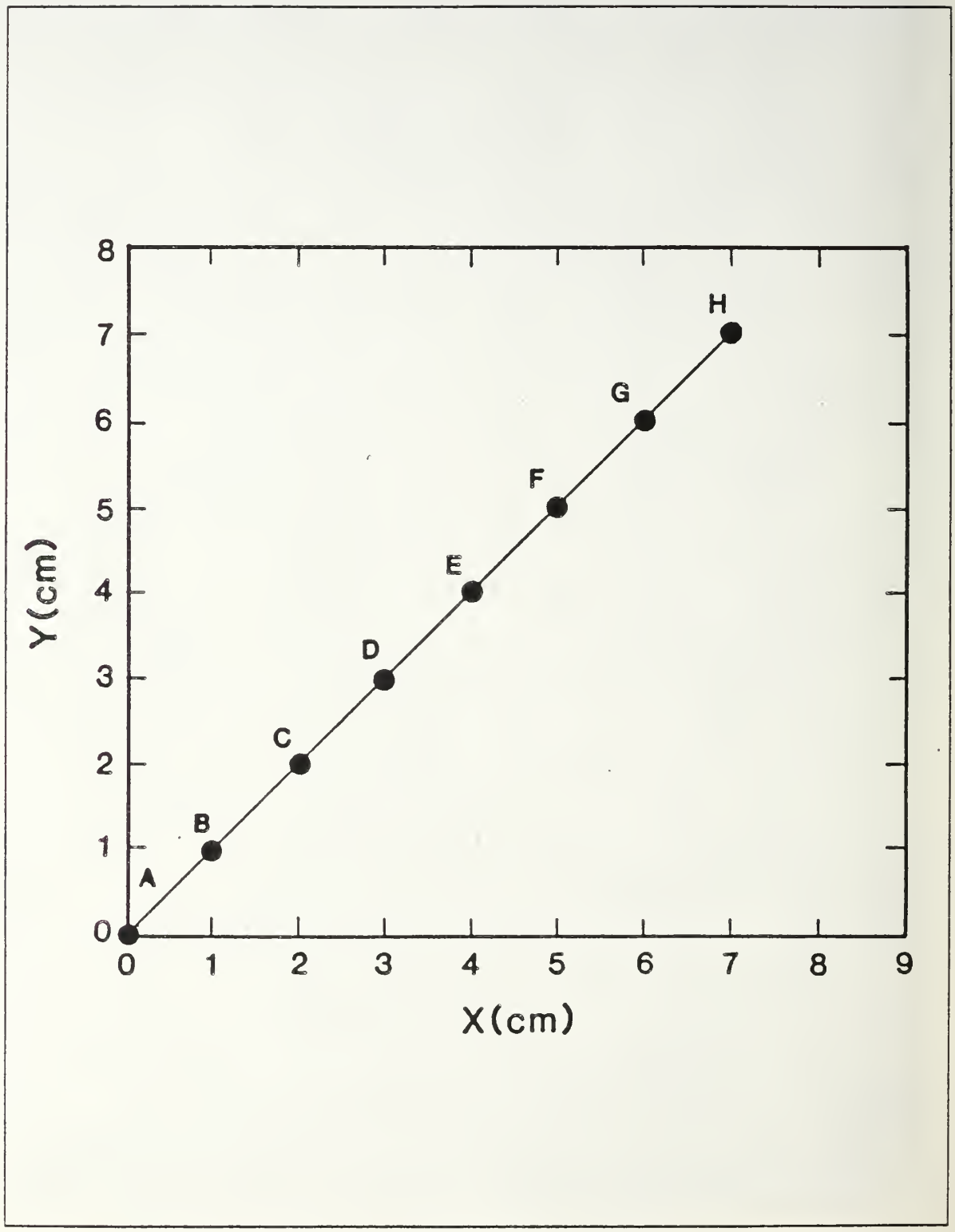

Figure 6. Pattern Used to Test the Enlargement Process

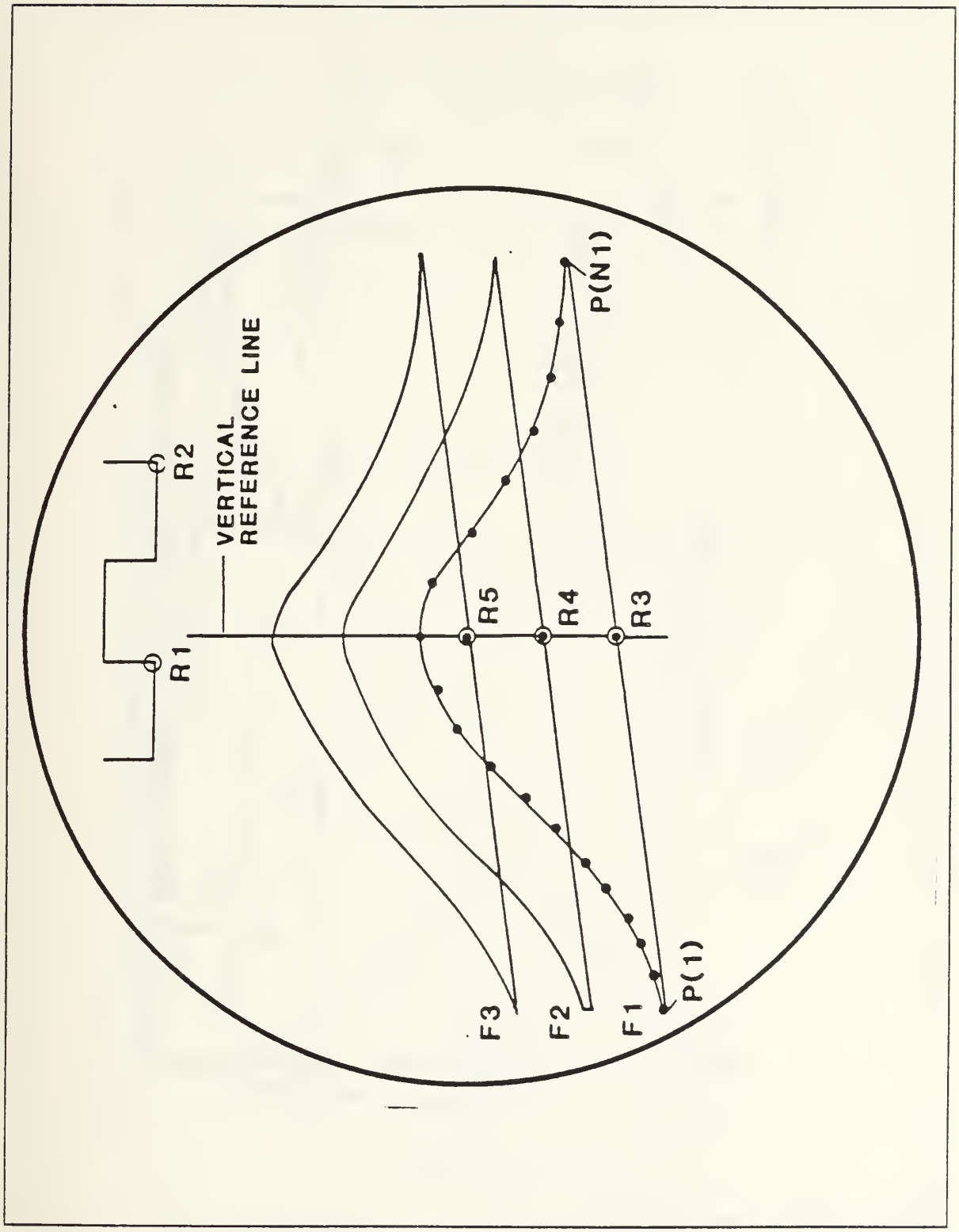

Figure 7. Sketch of Interferogram Prepared for Digitizing

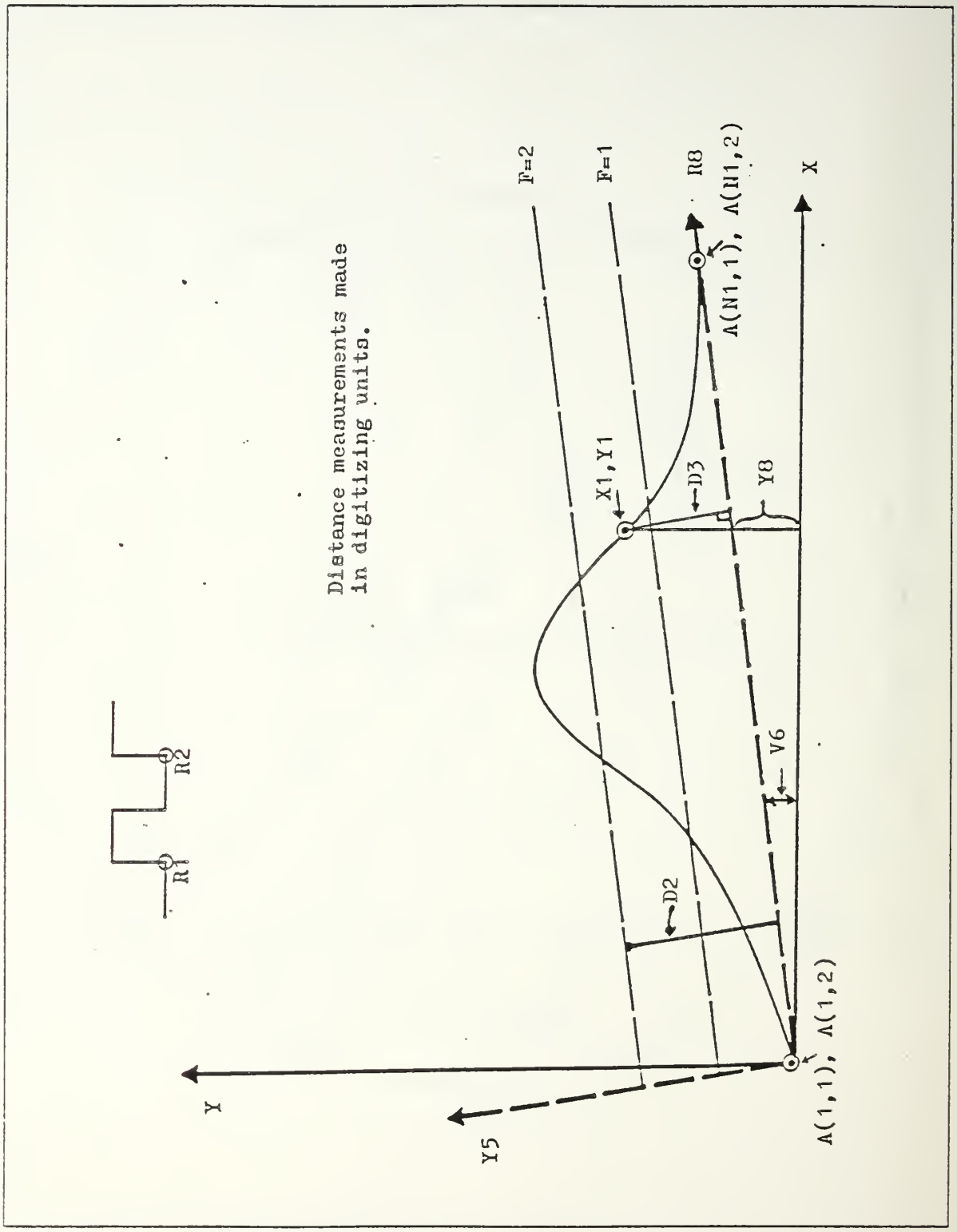

Figure 8. Sketch of Interferogram Annotated to Resolve Geometry

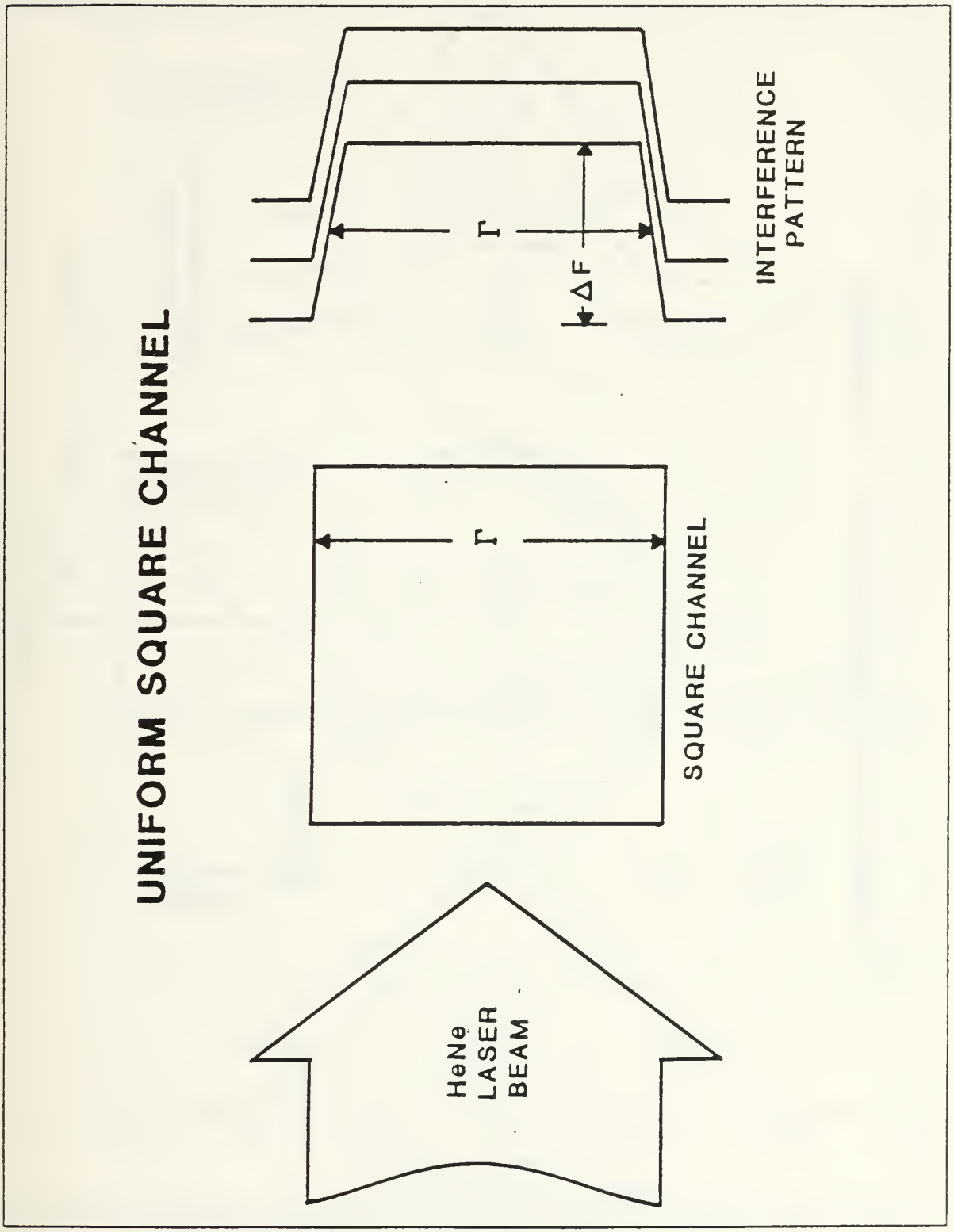

Figure 9. Sketch of Interferogram from Square Channel

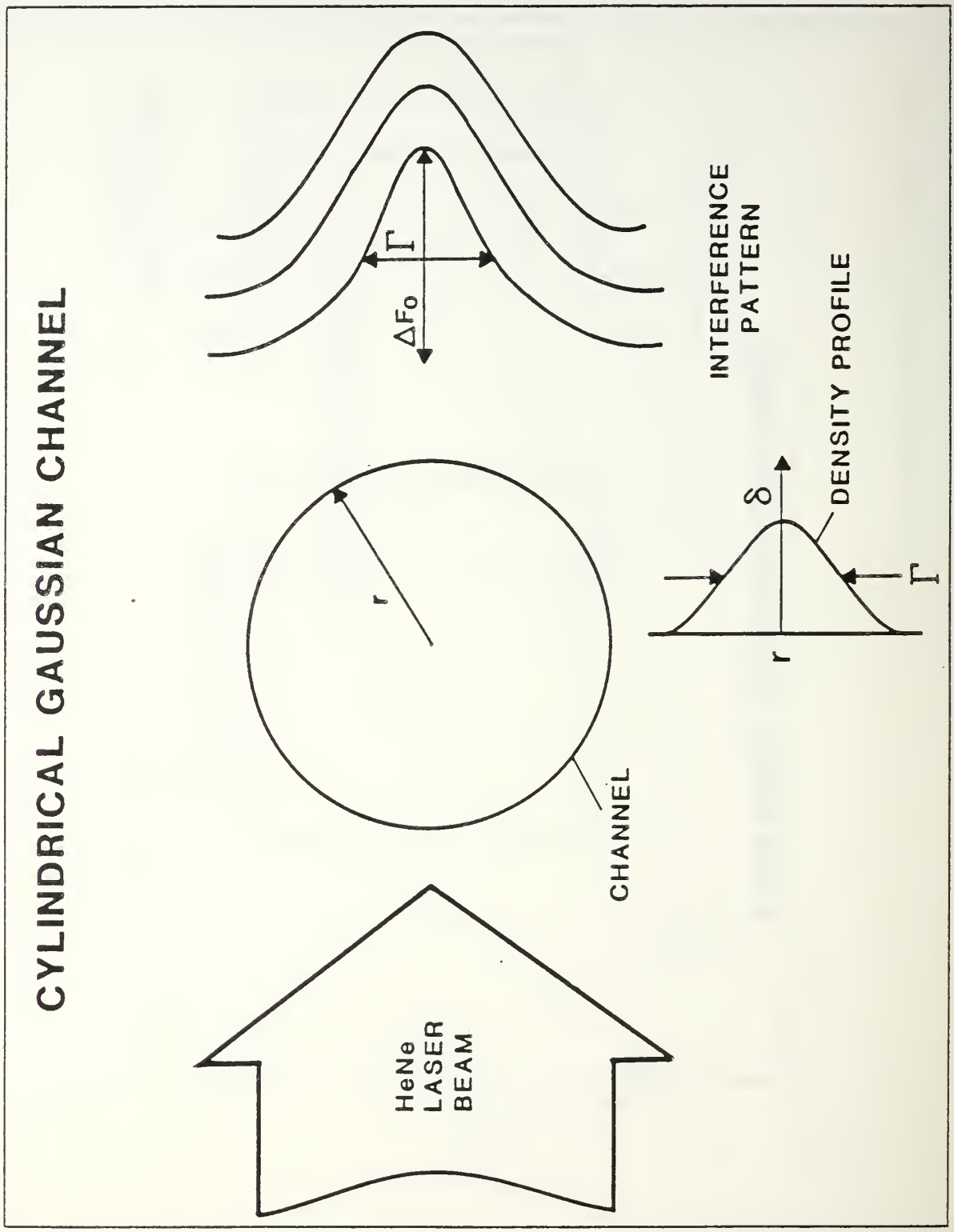

Figure 10. Sketch of Interferogram from Cylindrical Gaussian Channel

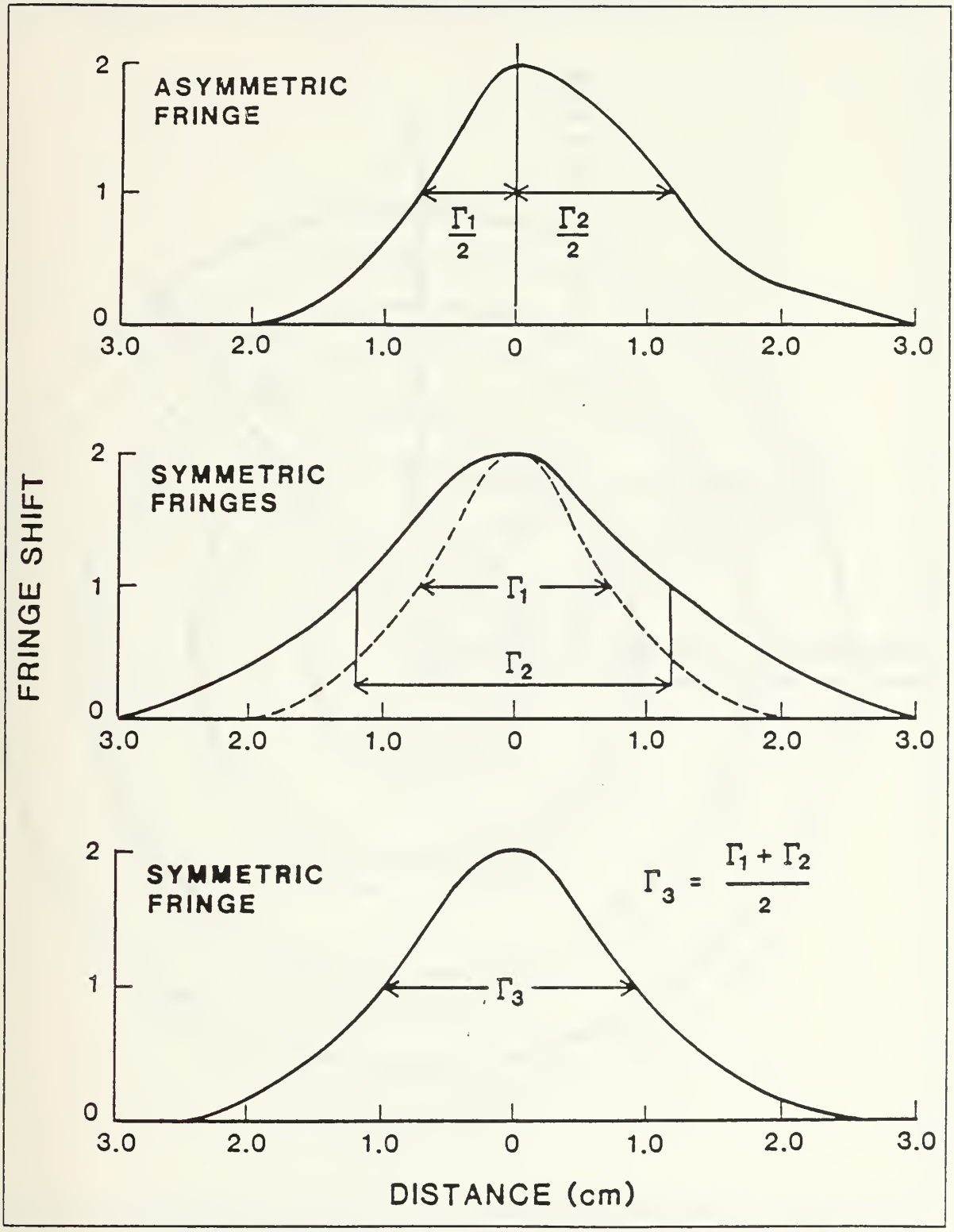

Figure 11. Sketch Showing Γ of Asymmetric Fringe Line

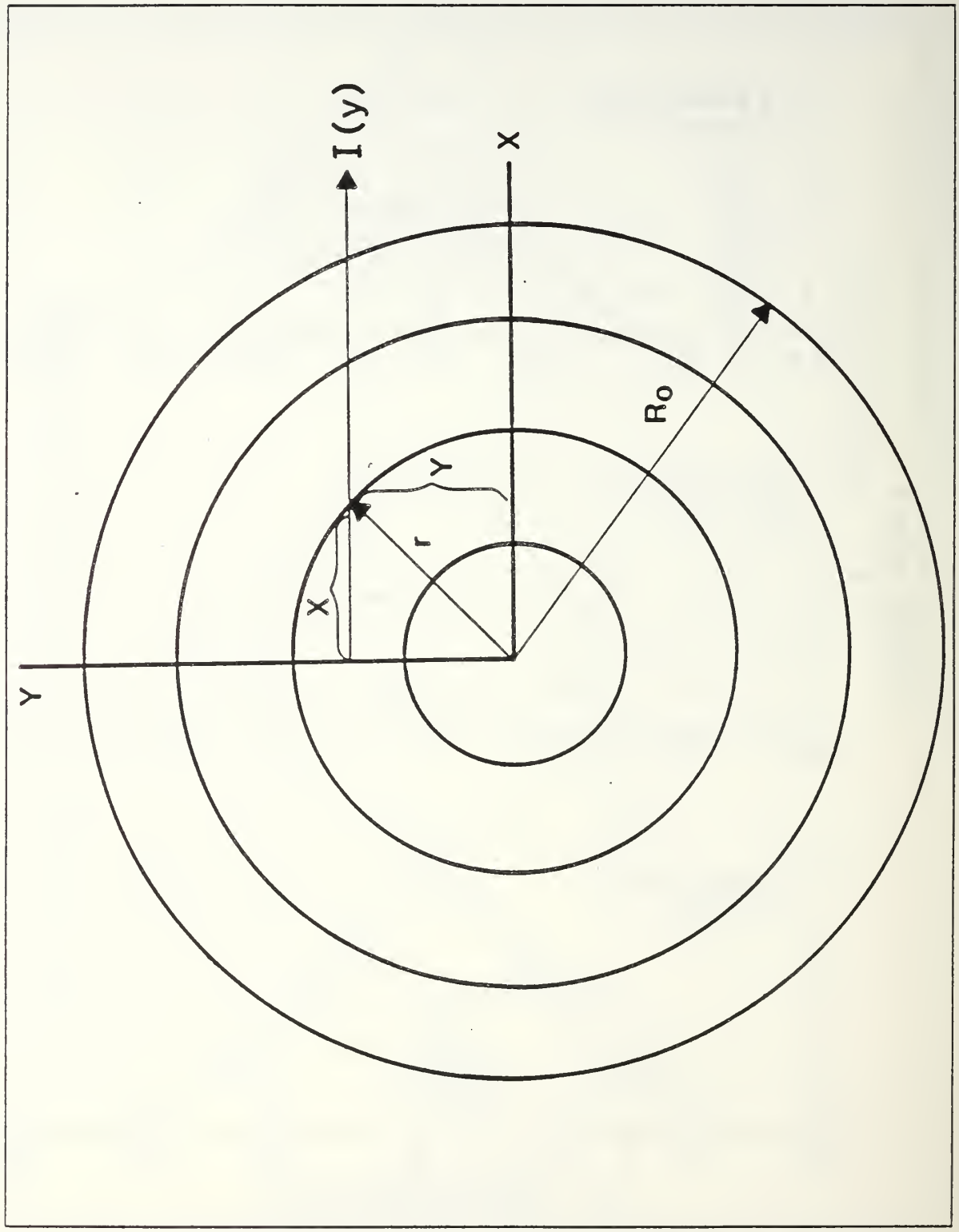

Figure 12. Schematic View of a Cylindrical Plasma Column

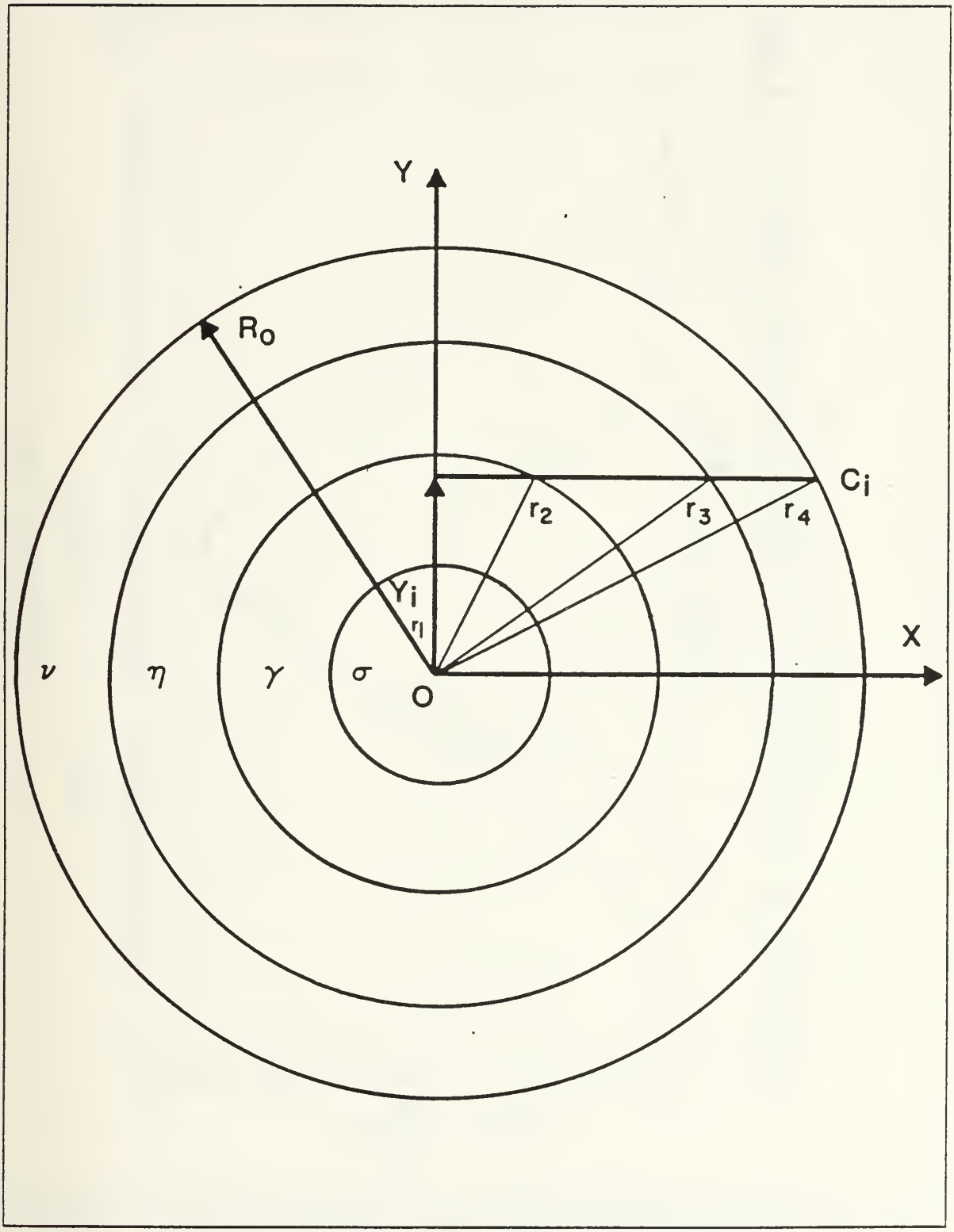

Figure 13. Cylindrically Symmetric Test Cell Containing NH3-N2 Gas Mixture

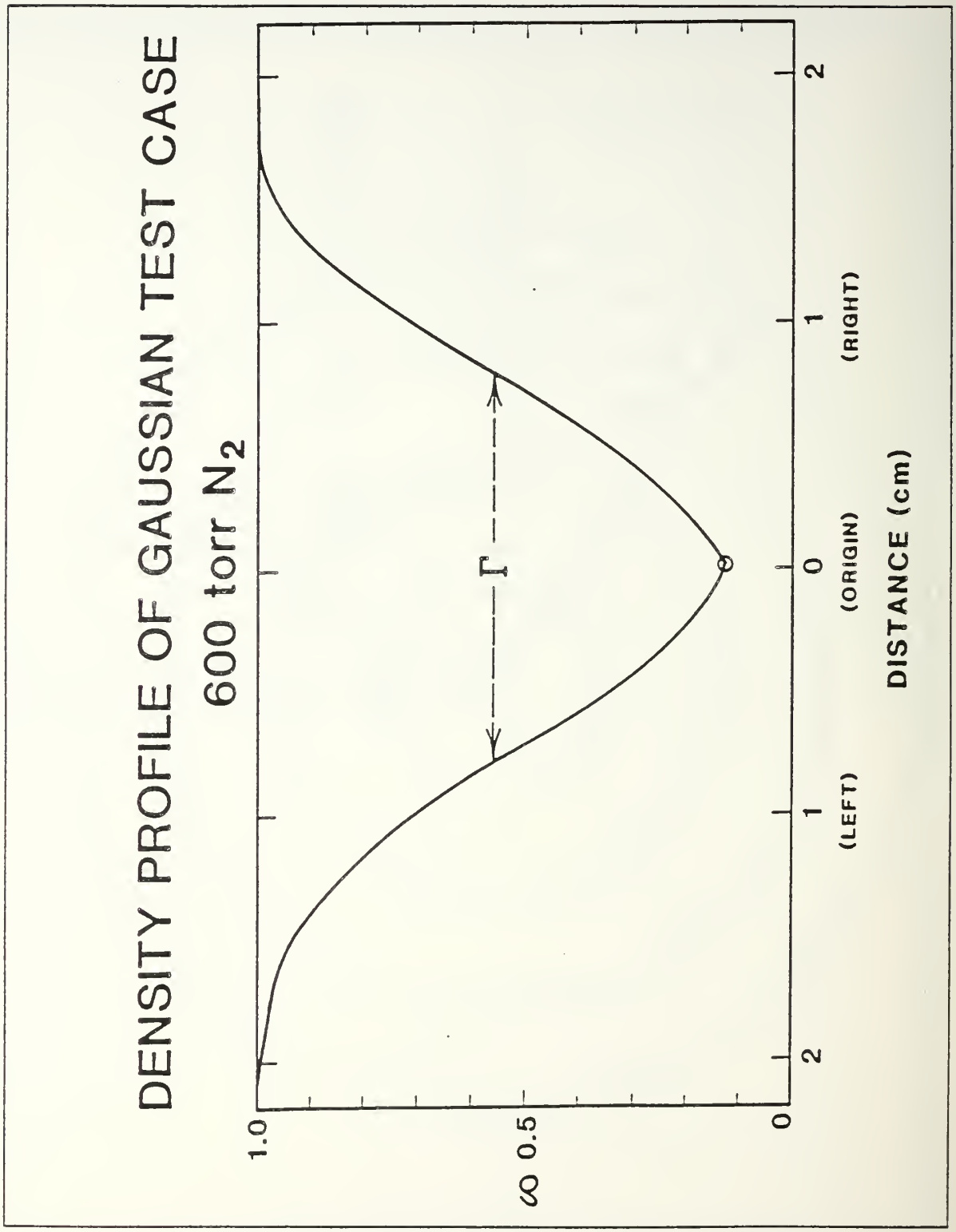

Figure 14. Abel Determined Density Profile of Gaussian Fringe Pattern

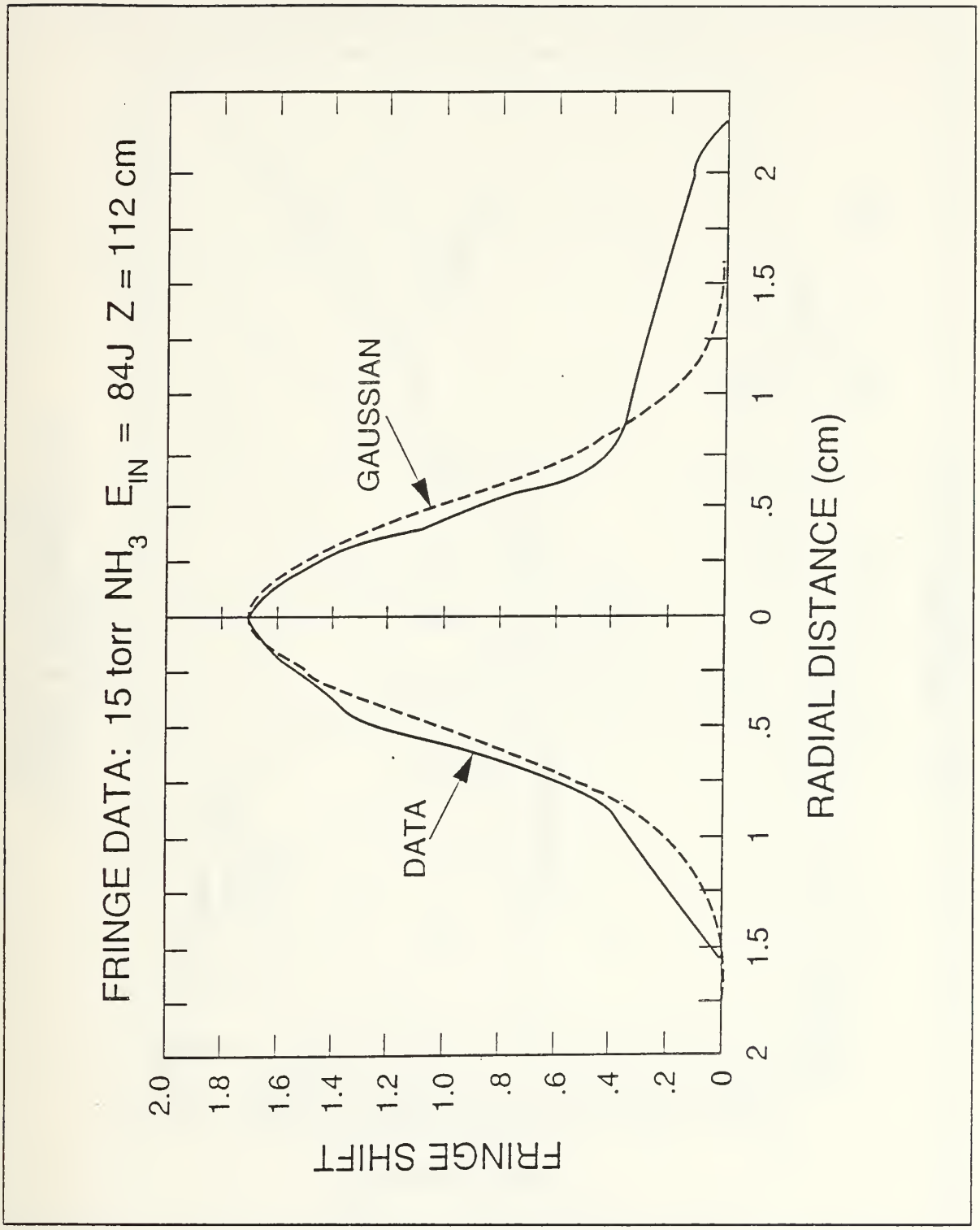

Figure 15. Comparison of Fringe Data to Gaussian Curve; Best Case.

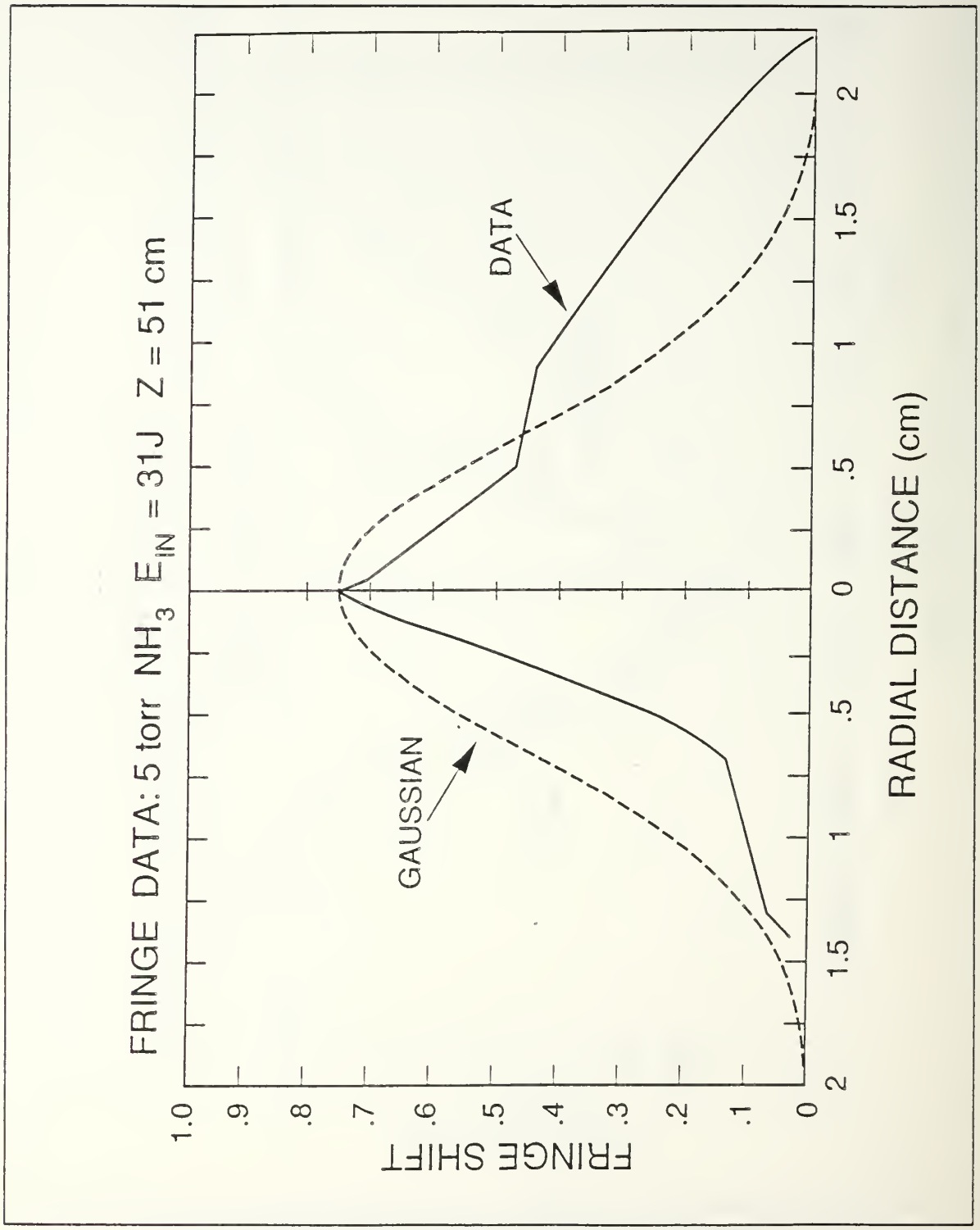

Figure 16. Comparison of Fringe Data to Gaussian Curve; Worst Case.

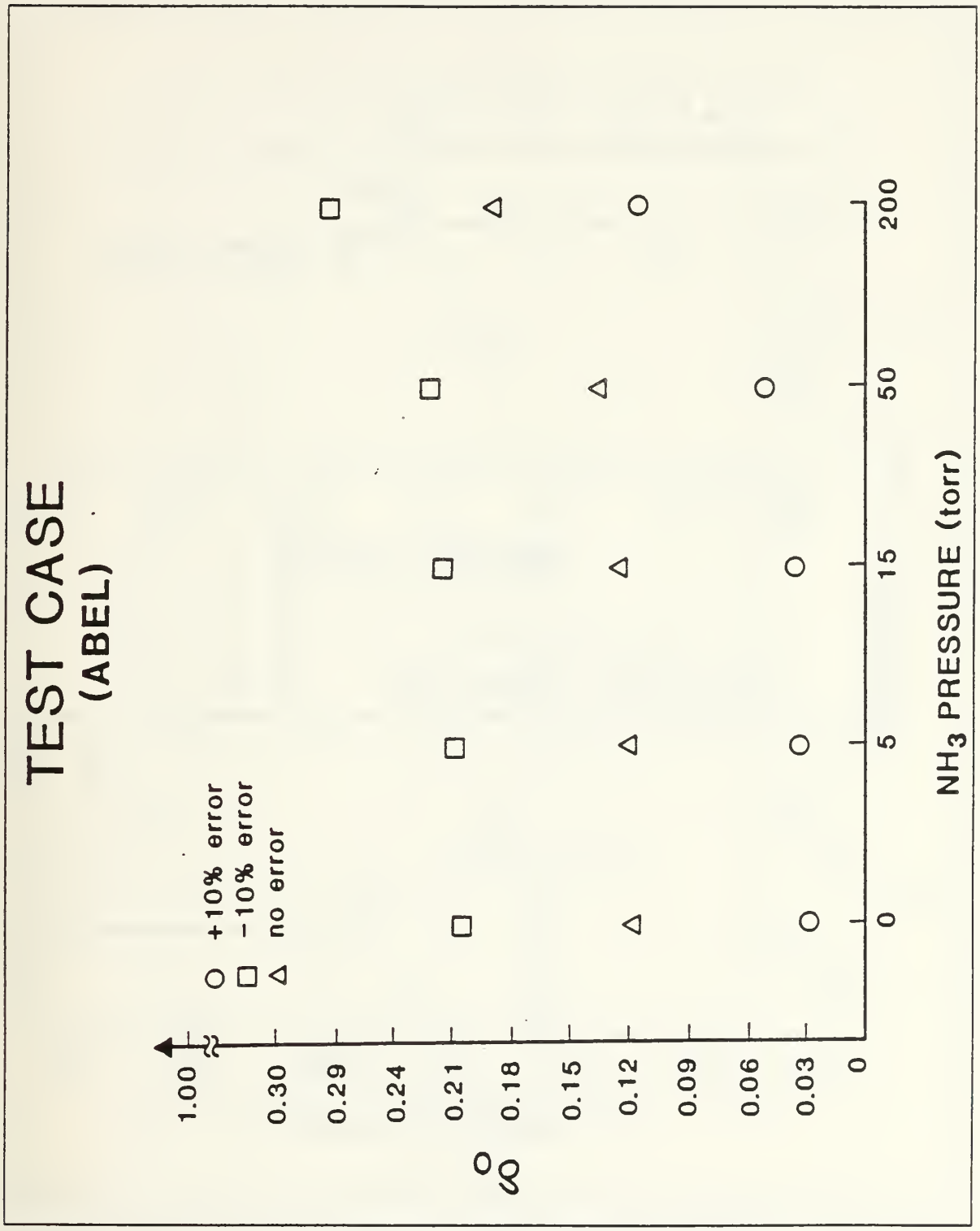

Figure 17. Plot of On-Axis Density (Abel) vs NH3 Concentration for Test Case and Test Case ± 10 Percent.

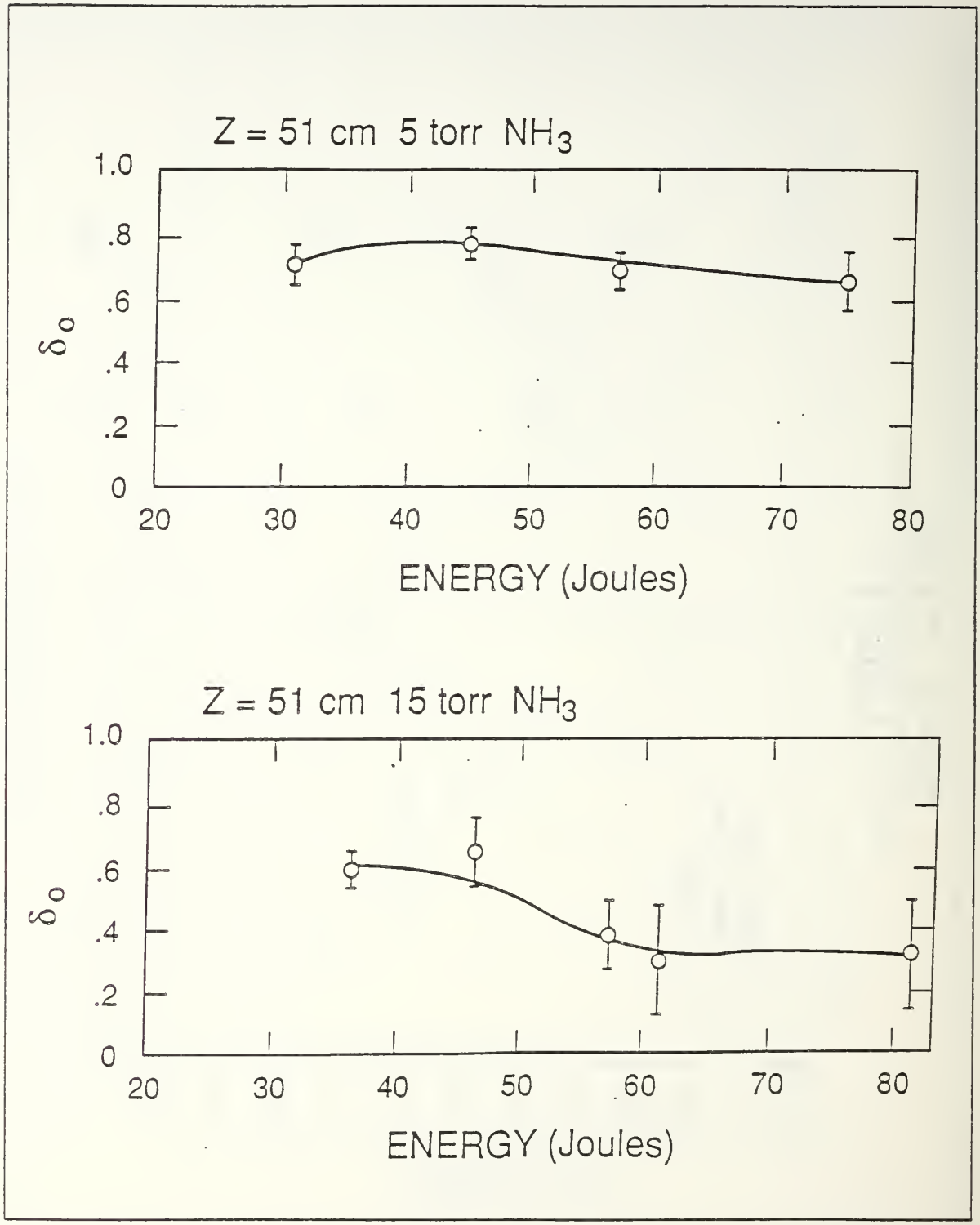

Figure 18. Variation of Channel Density with Laser Energy at 51 cm from Entrance of Test Cell for 5 torr NH3 (top), 15 torr NH3 (bottom).

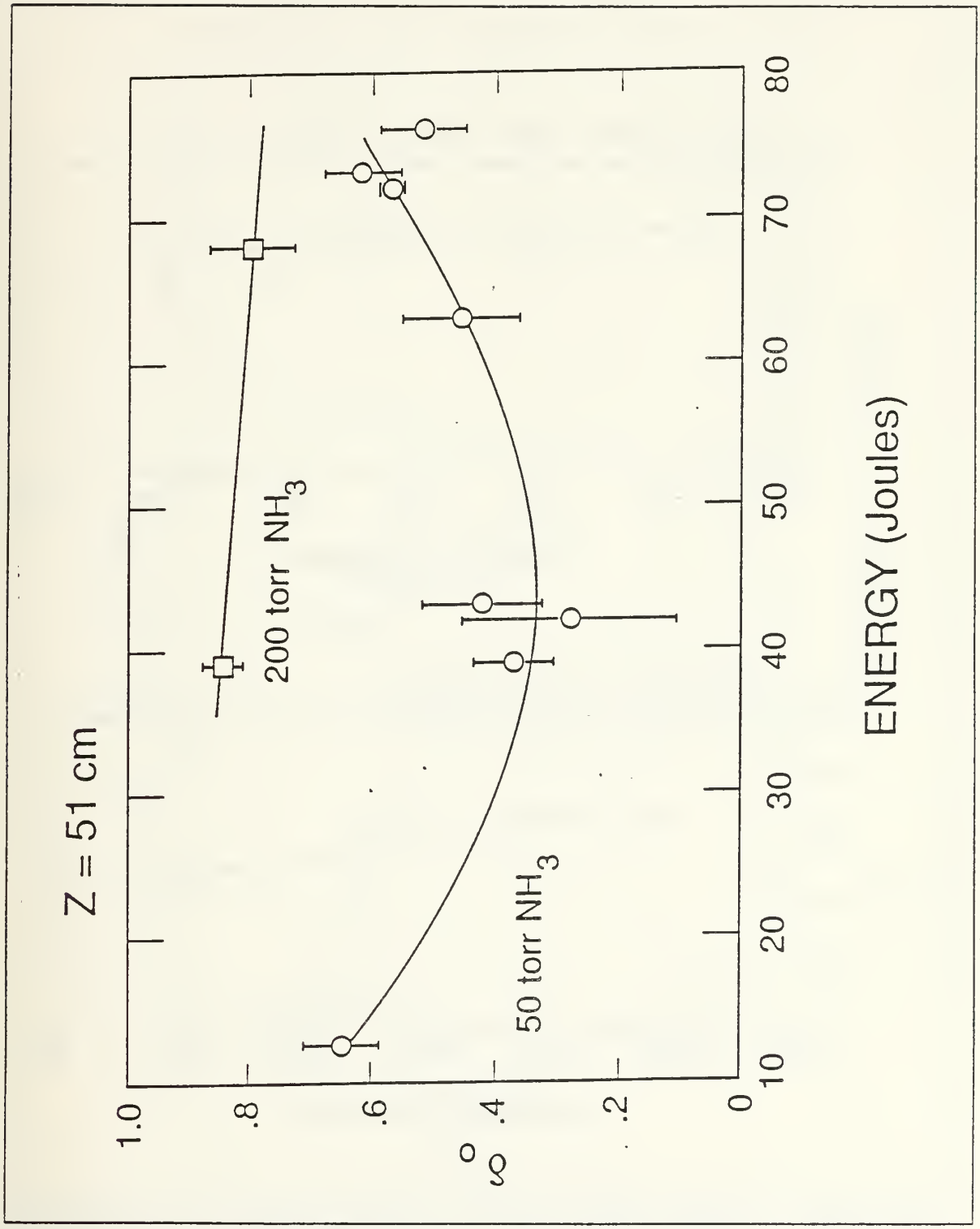

Figure 19. Variation of Channel Density with Laser Energy at 51 cm from Entrance of Test Cell for 50 torr NH3 (bottom), 200 torr (top).

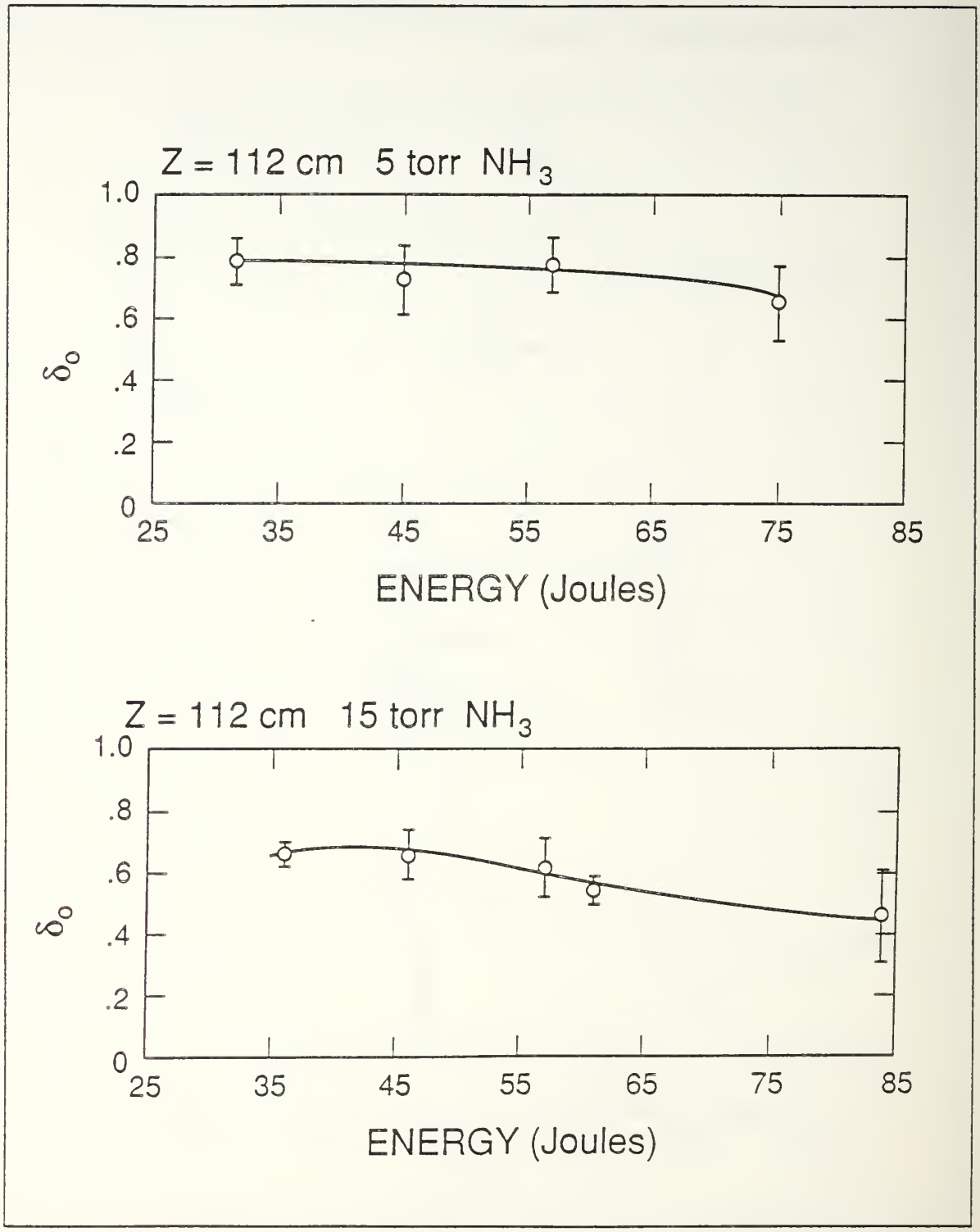

Figure 20. Variation of Channel Density with Laser Energy at 112 cm from Entrance of Test Cell for 5 torr NH3 (top), 15 torr NH3 (bottom).

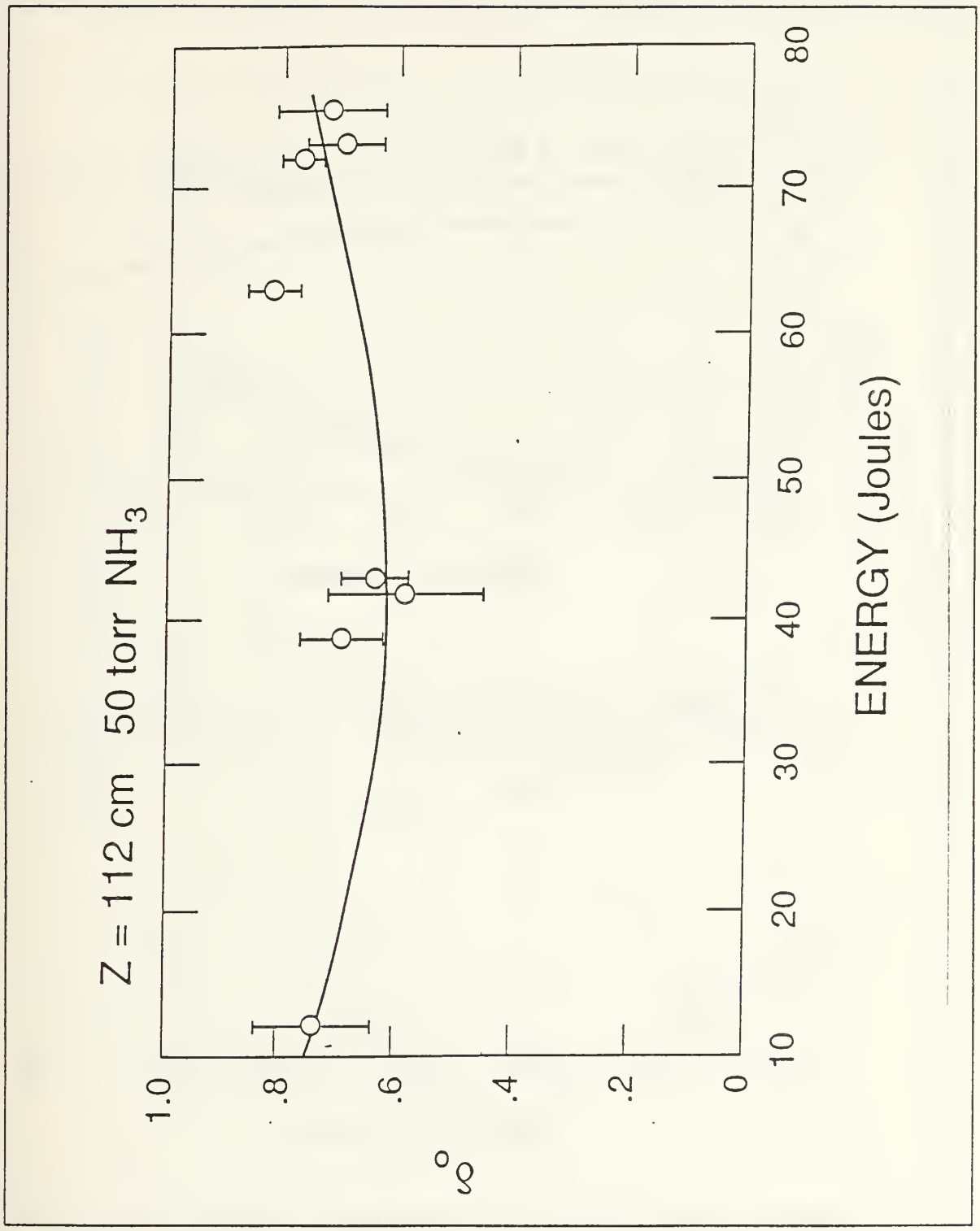

Figure 21. Variation of Channel Density with Laser Energy at 112 cm from Entrance of Test Cell for 50 torr NH3.

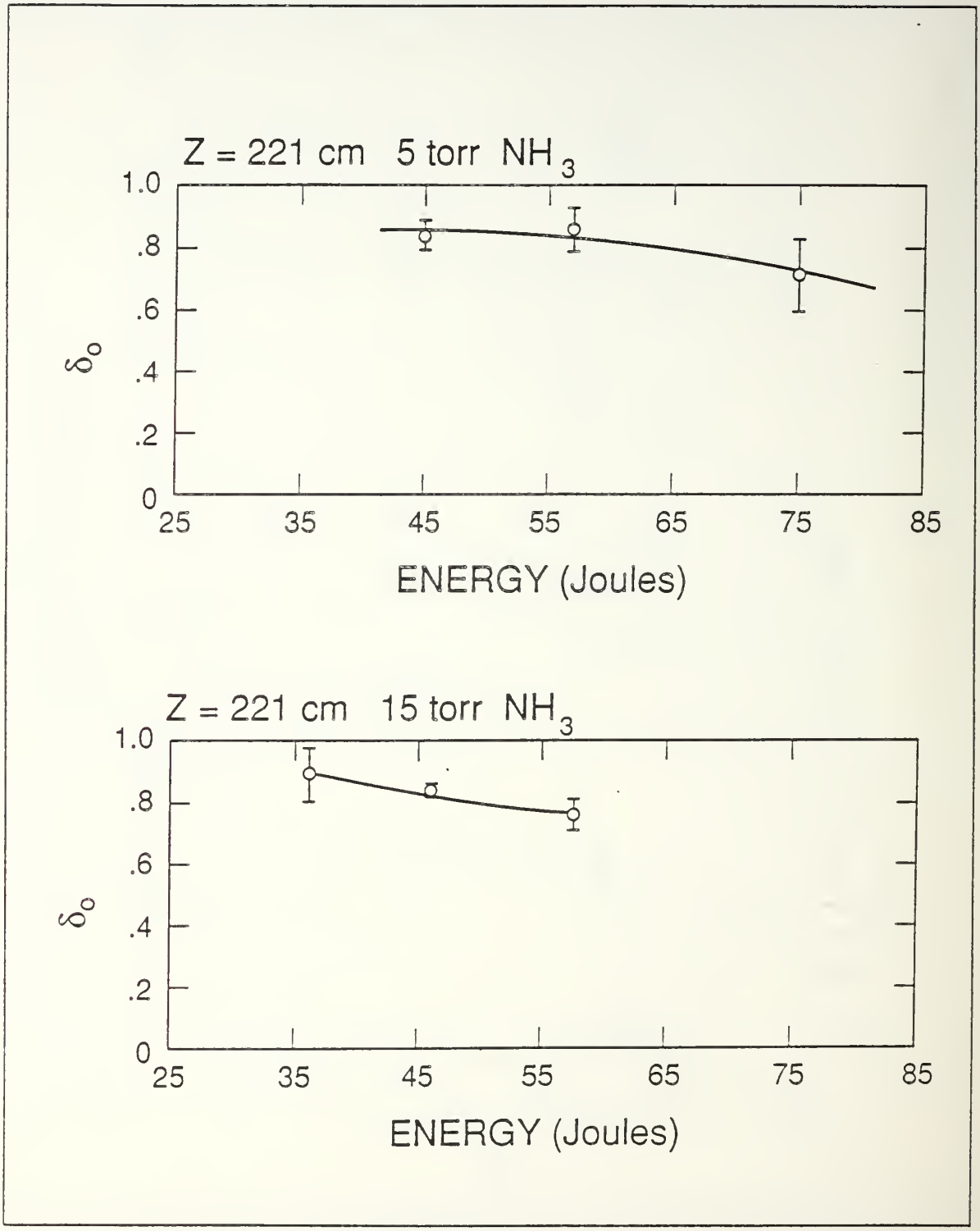

Figure 22. Variation of Channel Density with Laser Energy at 221 cm from Entrance of Test Cell for 5 torr NH3 (top), 15 torr NH3 (bottom).

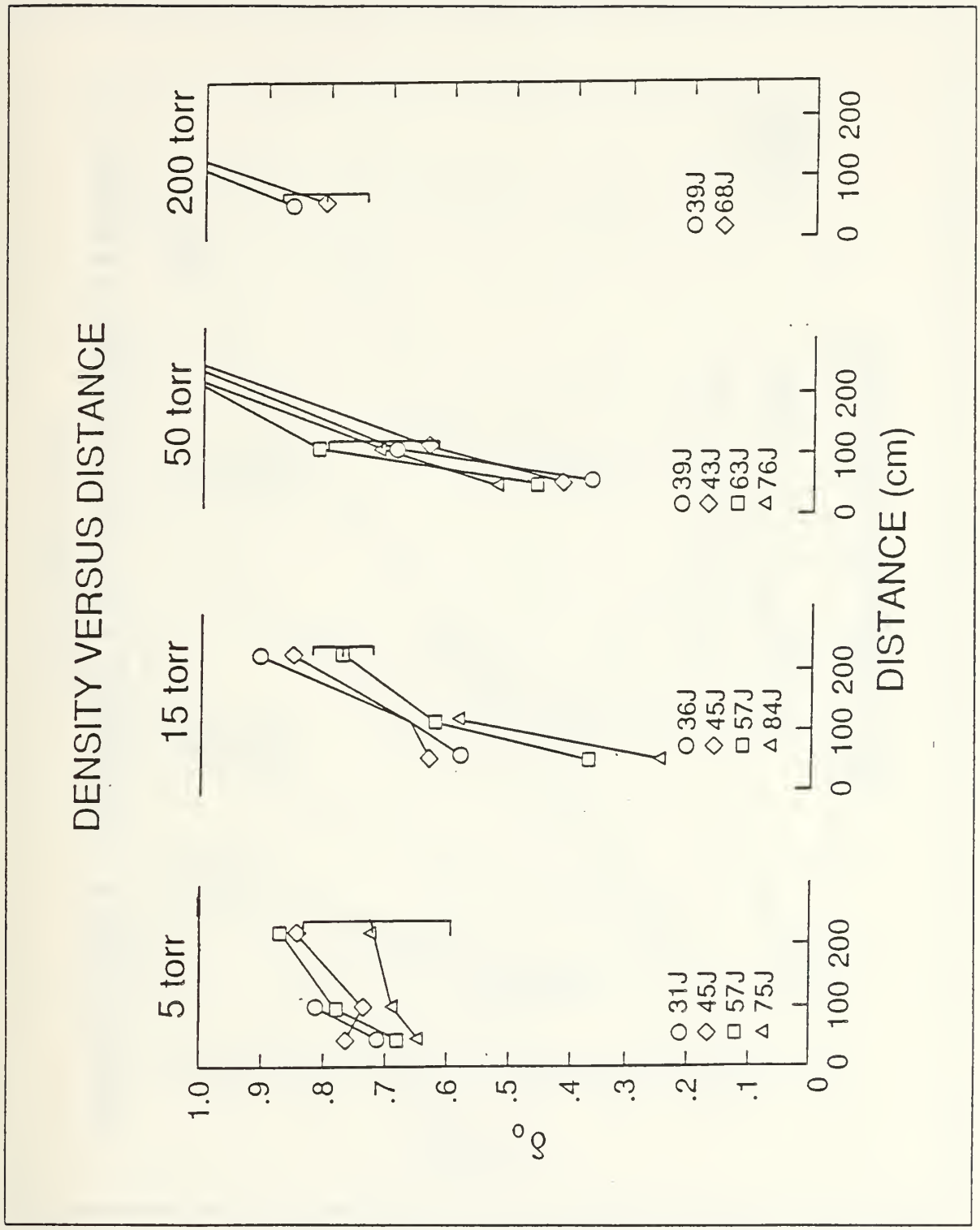

Figure 23. Variation of Channel Density with Distance from Test Cell Entrance for 5, 15, 50 and 200 torr NH3.

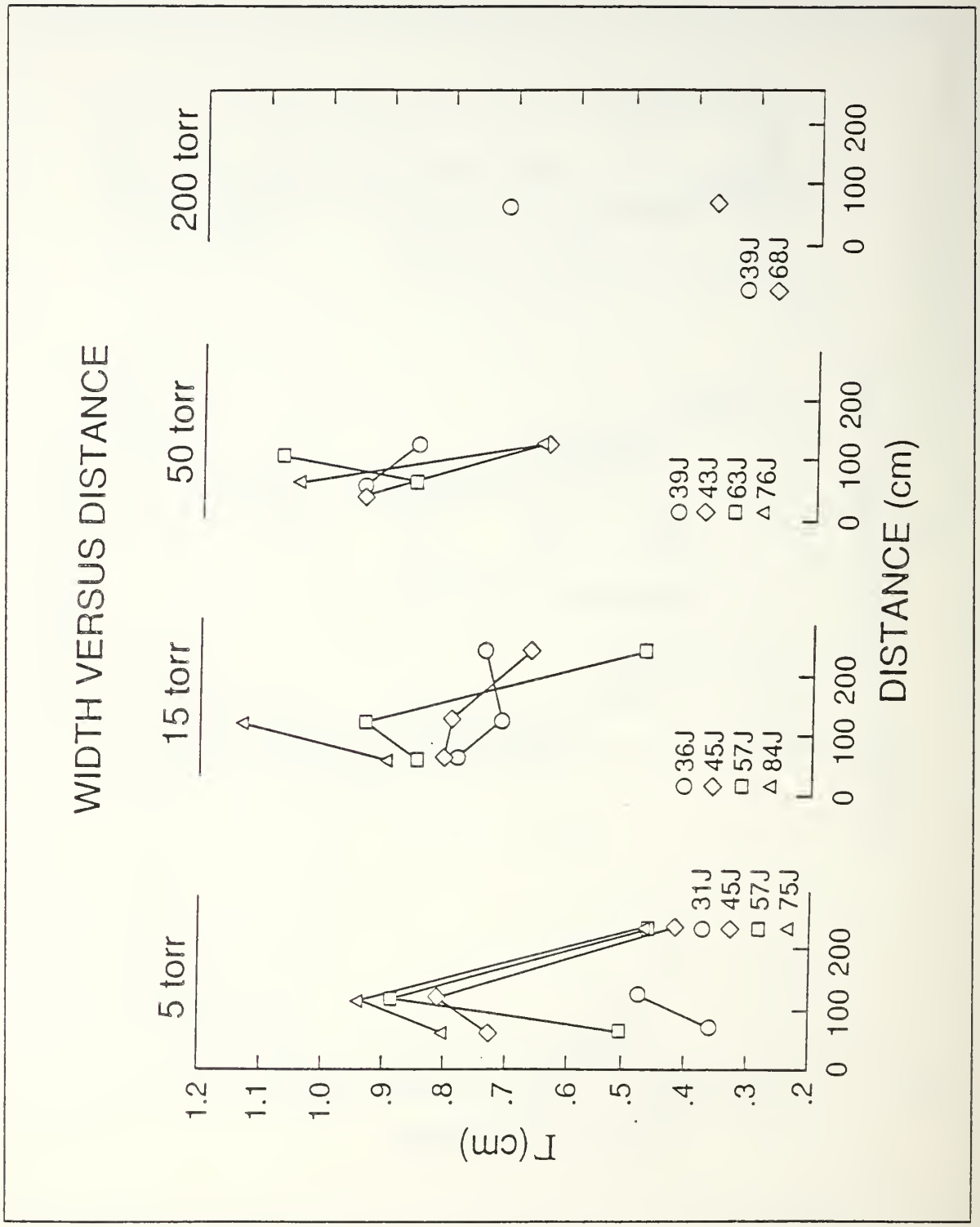

Figure 24. Variation of Channel Width with Distance from the Test Cell Entrance for 5, 15, 50 and 200 torr NH3.

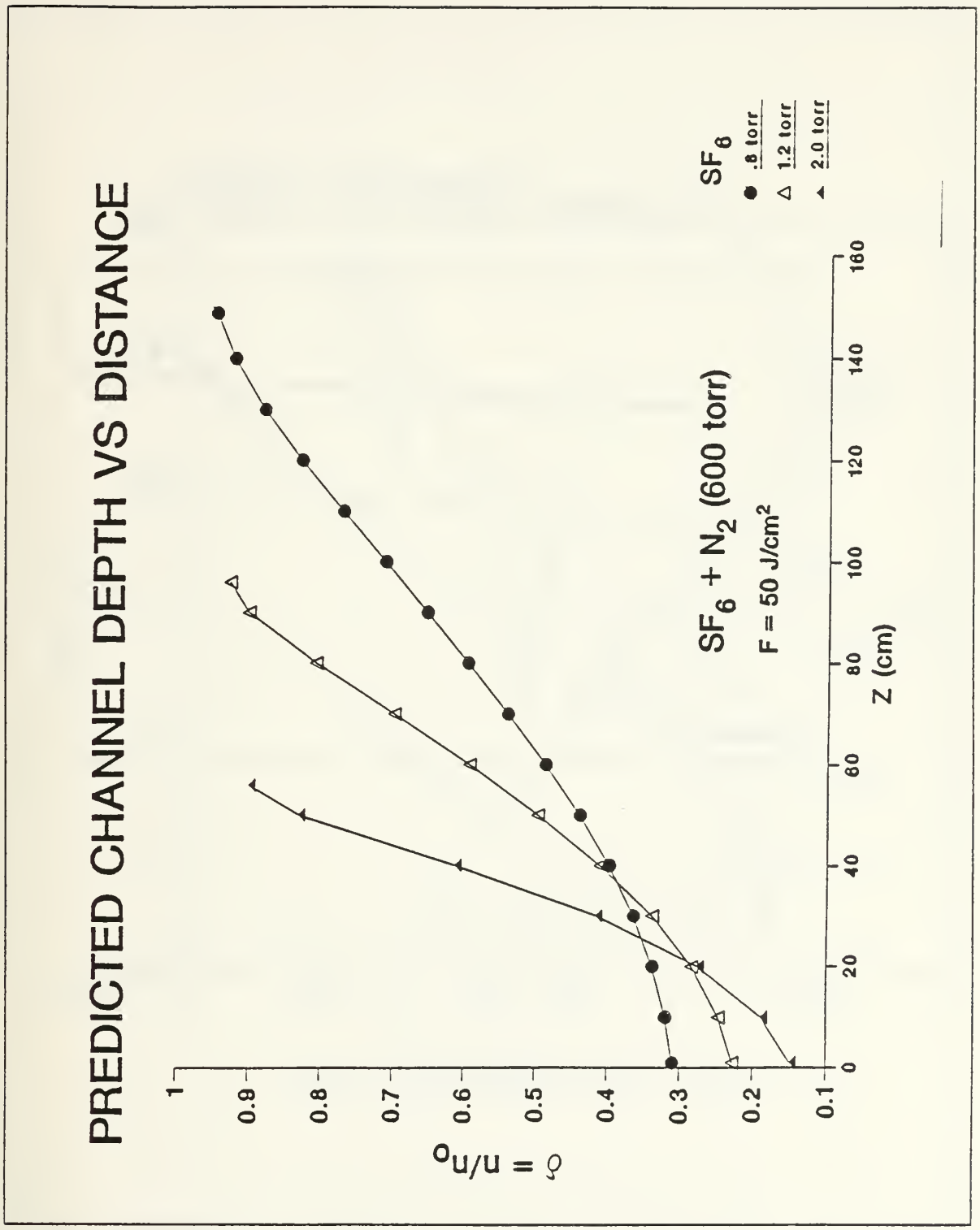

Figure 25. Predicted Channel Density for 50 joule Laser Energy for Concentrations of .8, 1.2 and 2.0 torr SF6.

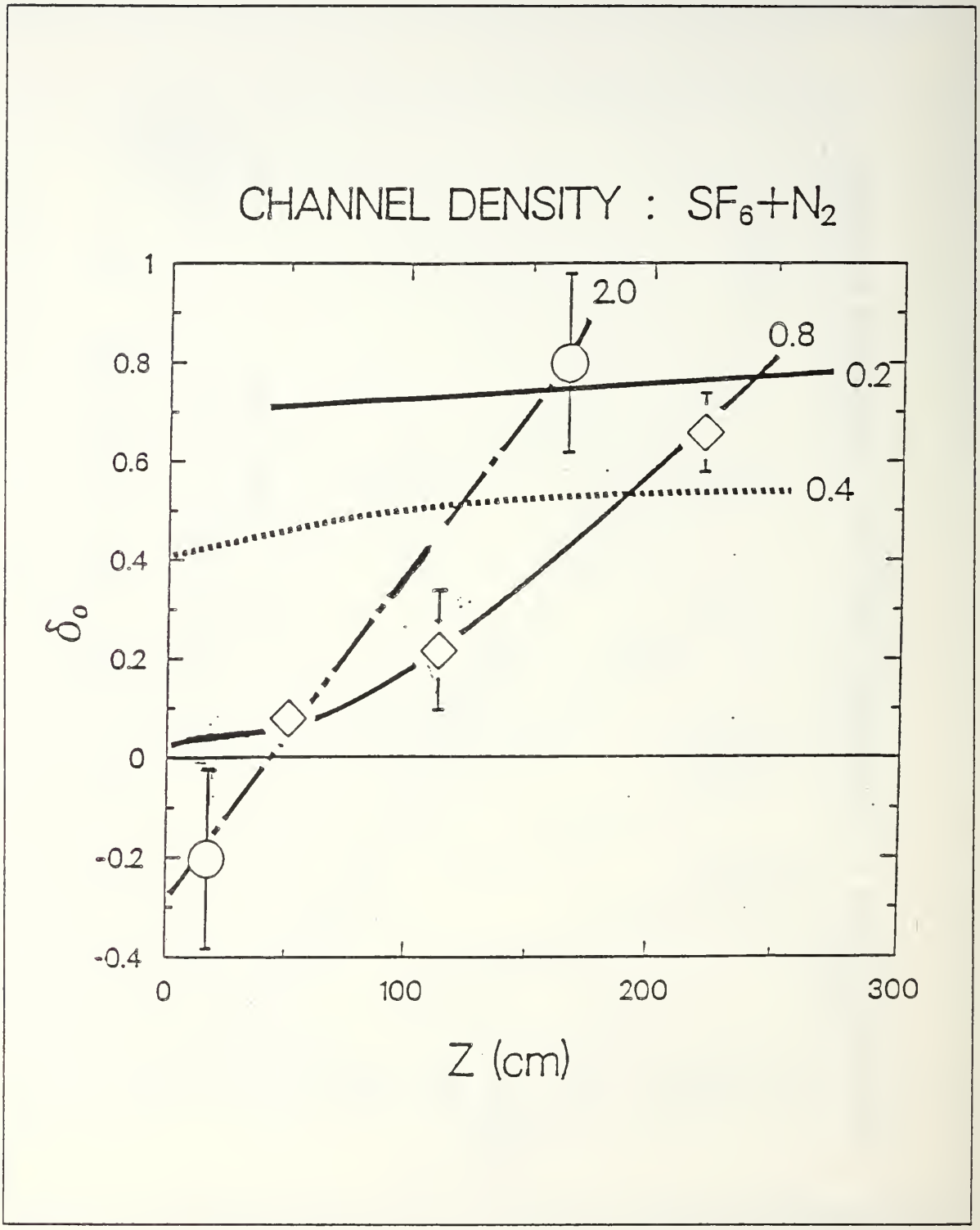

Figure 26. Variation of Channel Density with Distance from the Test Cell Entrance for 0.2, 0.4, 0.8 and 2.0 torr SF6.

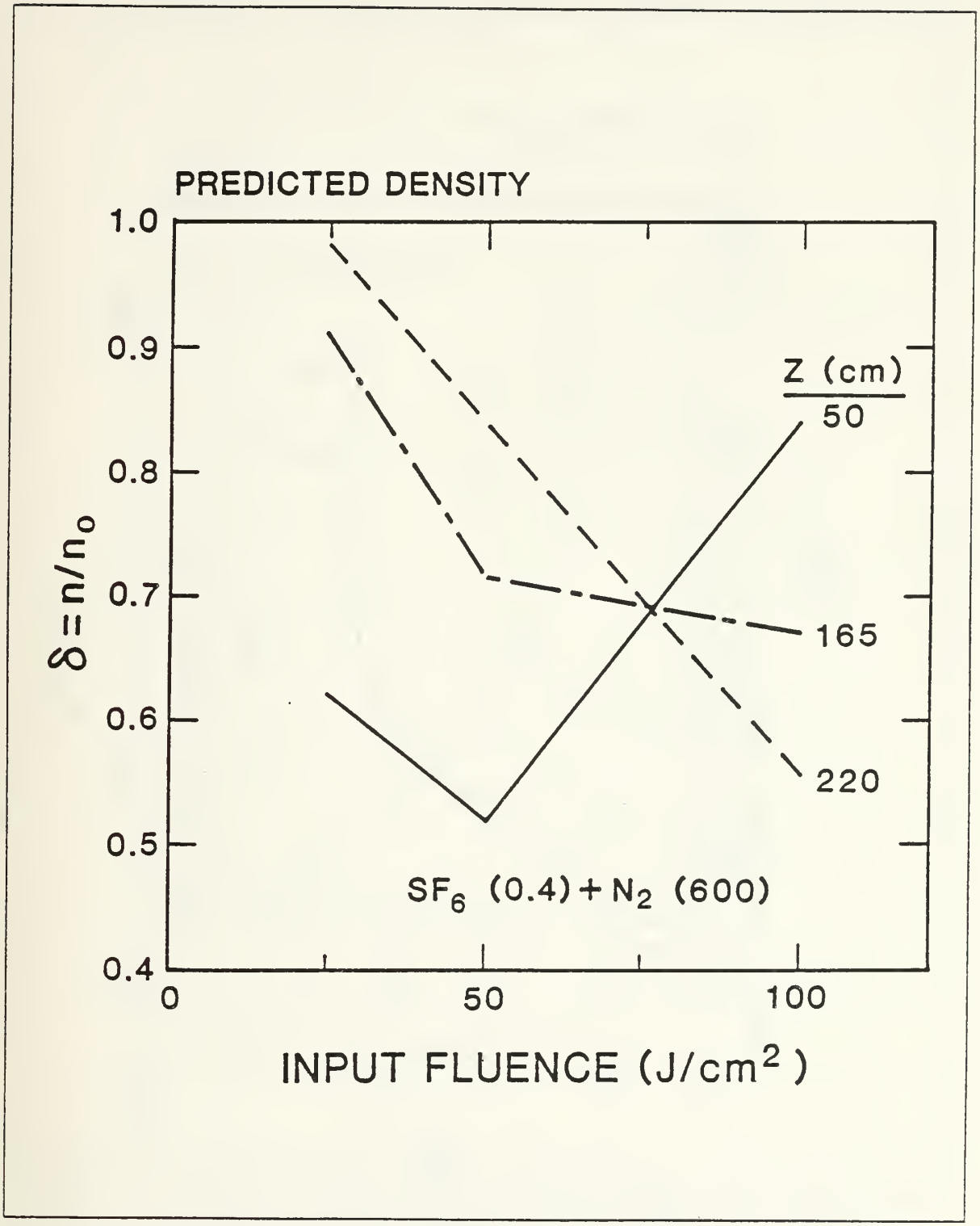

Figure 27. Predicted Variation of Channel Density with Laser Energy for 0.4 torr SF6 at 50, 165 and 220 cm from the Test Cell Entrance.

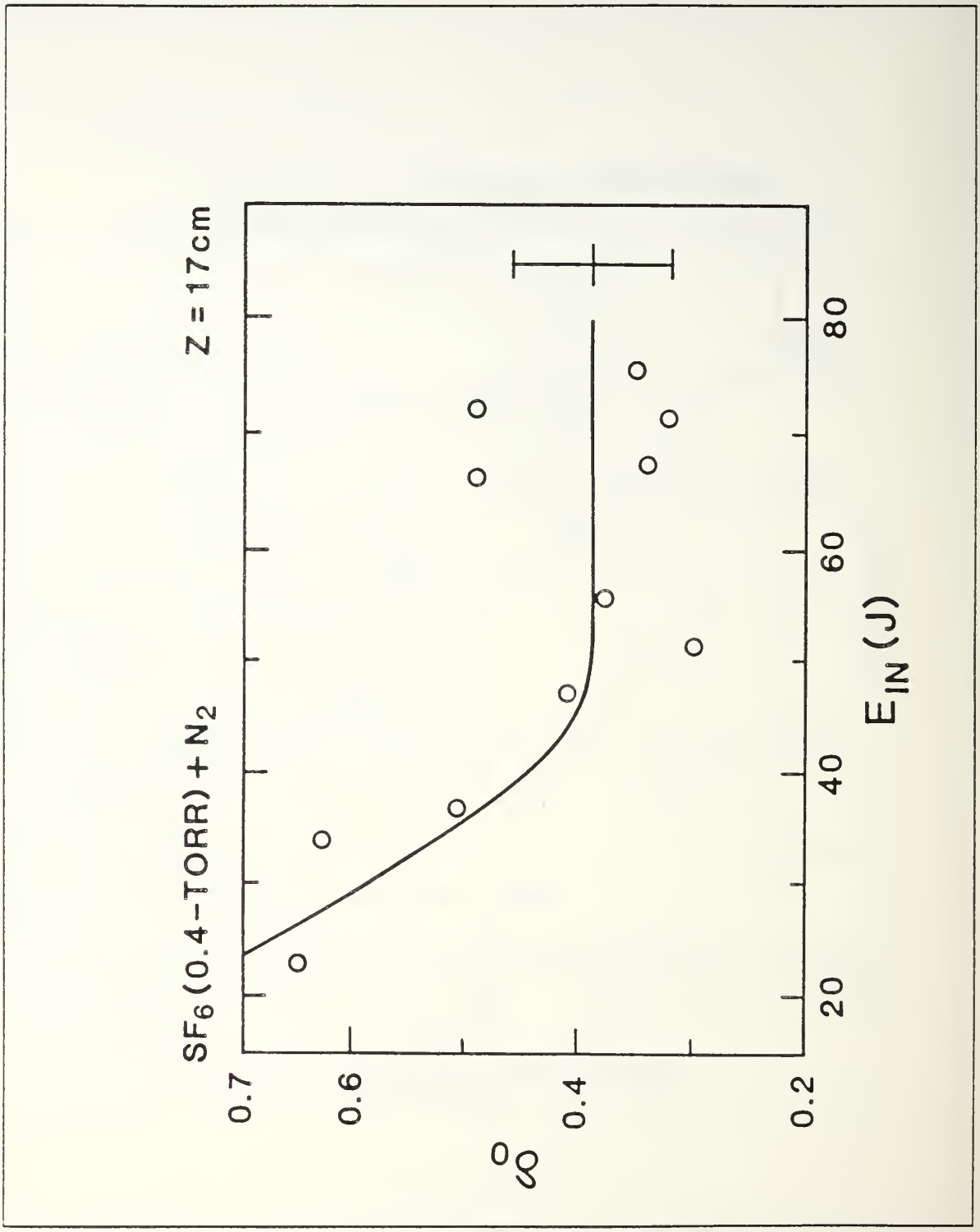

Figure 28. Variation of Channel Density with Laser Energy for 0.4 torr SF6 at 17 cm from the Test Cell Entrance.

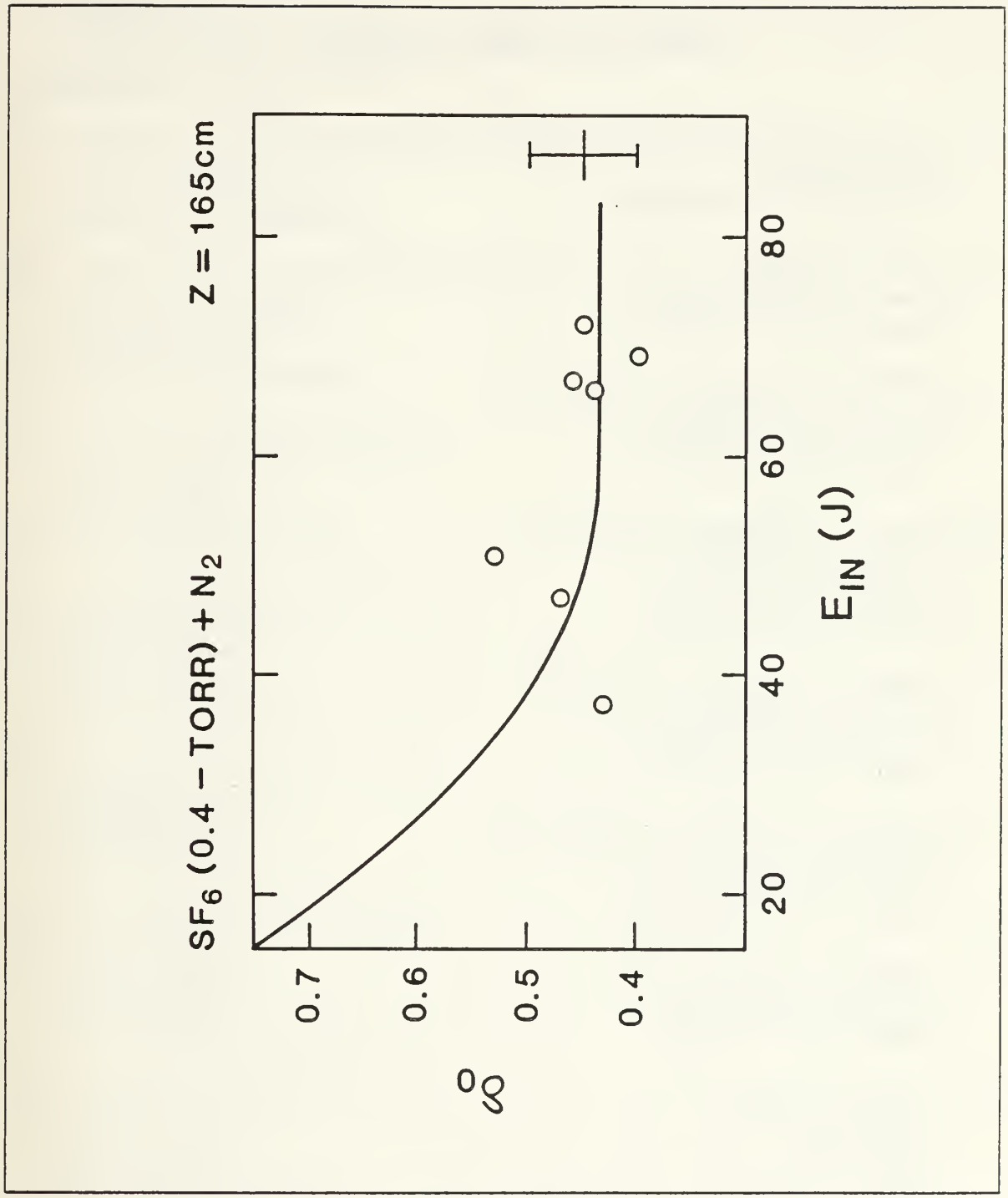

Figure 29. Variation of Channel Density with Laser Energy for 0.4 torr SF6 at 165 cm from the Test Cell Entrance.

INITIAL DISTRIBUTION LIST

		No. Copies
1.	Defense Technical Information Center Cameron Station Alexandria, VA 22304-6145	2
2.	Library, Code 0142 Naval Postgraduate School Monterey, CA 93943-5002	2
3.	Professor J.R. Neighbours, Code 61 Nb Department of Physics Naval Postgraduate School Monterey, CA 93943-5000	2
4.	Professor F.R. Buskirk, Code 61 Bs Department of Physics Naval Postgraduate School Monterey, CA 93943-5000	2
5.	Professor K.E. Woehler, Code 61 Wo Department of Physics Naval Postgraduate School Monterey, CA 93943-5000	2
6.	Professor X.M. Maruyama, Code 61 Mx Department of Physics Naval Postgraduate School Monterey, CA 93943-5000	2
7.	LCDR W.A. Goodwin 3100 Terra Grenada #2 Walnut Creek, CA 98545	2
8.	CPT Kurt Stevens AFTAC/TX OP Patrick AFB Patrick, FL 32925	1
9.	CAPT Fontana PMW-145 SPAWAR Washington, DC 20363-5100	1

10. Director, Defense Advanced Research Project Agency
ATTN: LCOL R.A. Gullickson
1400 Wilson Blvd.
Arlington, VA 22209-2308 — 2

11. Defense Advanced Research Project Agency
ATTN: Maj. G.P. Lasche
1400 Wilson Blvd.
Arlington, VA 22209-2308 — 1

12. Defense Advanced Research Project Agency
ATTN: Dr. Shen Shey
Directed Energy Office
1400 Wilson Blvd.
Arlington, VA 22209-2308 — 1

13. Los Alamos National Laboratory
ATTN: Dr. Randolph Carlson
Mail Stop P942
P.O. Box 1663
Los Alamos, NM 87545 — 1

14. Los Alamos National Laboratory
ATTN: Dr. David Moir
Mail Stop P942
P.O. Box 1663
Los Alamos, NM 87545 — 1

15. Los Alamos National Laboratory
ATTN: Dr. T. Neal
Mail Stop P942
P.O. Box 1663
Los Alamos, NM 87545 — 1

16. Los Alamos National Laboratory
ATTN: Dr. S. J. Czuchlewski
Mail Stop E543
P.O. Box 1663
Los Alamos, NM 87545 — 1

17. Los Alamos National Laboratory
ATTN: Dr. J. Mack
Mail Stop E554
P.O. Box 1663
Los Alamos, NM 87545 — 1

18. Mission Research Corporation
ATTN: Dr. D. Mitrovitch
Plasma Sciences Division
1720 Randolph Road, SE
Albbuquerque, NM 87106 — 1

19. Naval Research Laboratory
ATTN: Dr. J.R. Greig (4763)
4555 Overlook Avenue, SW
Washington, DC 20375 — 1

20. Naval Research Laboratory
ATTN: Dr. R. Hubbard (4790)
4555 Overlook Avenue, SW
Washington, DC 20375 — 1

21. Naval Research Laboratory
ATTN: Dr. A. Wahab Ali (4700.1)
4555 Overlook Avenue, SW
Washington, DC 20375 — 1

22. Naval Research Laboratory
ATTN: Dr. R. Pechacek (4760)
4555 Overlook Avenue, SW
Washington, DC 20375 — 1

23. Naval Research Laboratory
ATTN: Dr. D. Murphy (4760)
4555 Overlook Avenue, SW
Washington, DC 20375 — 1

24. Naval Research Laboratory
ATTN: Dr. M. Raleigh (4760)
4555 Overlook Avenue, SW
Washington, DC 20375 — 1

25. Naval Research Laboratory
ATTN: Dr. R. Fernsler (4770)
4555 Overlook Avenue, SW
Washington, DC 20375 — 1

26. Naval Research Laboratory
ATTN: Dr. B. Hui (4790)
4555 Overlook Avenue, SW
Washington, DC 20375 — 1

27. Naval Research Laboratory
ATTN: Dr. G. Joyce (4790)
4555 Overlook Avenue, SW
Washington, DC 20375 — 1

28. Naval Surface Weapons Center
White Oak Laboratory
ATTN: Dr. E.E. Nolting (R401)
10901 New Hampshire Avenue
Silver Spring, MD 20903-5000 — 1

29. Naval Surface Weapons Center
White Oak Laboratory
ATTN: Dr. A. Smith (H23)
10901 New Hampshire Avenue
Silver Spring, MD 20903-5000 — 1

30. Naval Surface Weapons Center
White Oak Laboratory
ATTN: Dr. H.C. Chen (R41)
10901 New Hampshire Avenue
Silver Spring, MD 20903-5000 — 1

31. Naval Surface Weapons Center
White Oak Laboratory
ATTN: Dr. H.S. Uhm (R41)
10901 New Hampshire Avenue
Silver Spring, MD 20903-5000 — 1

32. Naval Surface Weapons Center
White Oak Laboratory
ATTN: Dr. R. Fiorito (R41)
10901 New Hampshire Avenue
Silver Springs, MD 20903-5000 — 1

33. Naval Surface Weapons Center
White Oak Laboratory
ATTN: Dr. J. Smith (R41)
10901 New Hampshire Avenue
Silver Springs, MD 20903-5000 — 1

34. Naval Surface Weapons Center
White Oak Laboratory
ATTN: Dr. D. Rule (R41)
10901 New Hampshire Avenue
Silver Spring, MD 20903-5000 — 1

35. Naval Surface Weapons Center
White Oak Laboratory
ATTN: Dr. M.J. Rhee (R41)
10901 New Hampshire Avenue
Silver Spring, MD 20903-5000 — 1

36. Office of Naval Research
ATTN: CDR James Offutt
1030 East Green Street
Pasadena, CA 91106 — 1

37. Office of Naval Research
ATTN: CDR R. Swafford
800 N. Quincy Street
Arlington, VA 22217 — 1

38. Admiral R.L. Topping 1
Space and Naval Warfare Systems Command
SPAWAR-06
Washington, DC 20363-5100

39. LCDR E. Turner 1
PMW-145
SPAWAR
Washington, DC 20363-5100

40. Sandia National Laboratories 1
ATTN: Dr. C. Ekdahl (1272)
P.O. Box 5800
Albequerque, NM 87185

41. Sandia National Laboratories 1
ATTN: Dr. R. Lipinski (1272)
P.O. Box 5800
Albequerque, NM 87185

42. Sandia National Laboratories 1
ATTN: Dr. M. Mazarakis (1272)
P.O. Box 5800
Albequerque, NM 87185

43. Sandia National Laboratories 1
ATTN: Dr. D. Hasti
P.O. Box 5800
Albequerque, NM 87185

44. Sandia National Laboratories 1
ATTN: Dr. C. Frost
P.O. Box 5800
Albequerque, NM 87185

45. Sandia National Laboratories 1
ATTN: Dr. J. Freeman (1241)
P.O. Box 5800
Albequerque, NM 87185

46. Sandia National Laboratories 1
ATTN: Dr. G.T. Leifeste (1241)
P.O. Box 5800
Albequerque, NM 87185

47. Dr. K.W. Struve 1
Lawrence Livermore National Laboratory
P.O. Box 808
Livermore, CA 94550

DUDLEY KNOX LIBRARY
NAVAL POSTGRADUATE SCHOOL
MONTEREY, CALIFORNIA 93943-5002

Thesis
G57333 Goodwin
c.2 The characteristics of reduced-density channels in NH3-N2 gas mixtures.

Thesis
G57333 Goodwin
c.2 The characteristics of reduced-density channels in NH3-N2 gas mixtures.

DUDLEY KNOX LIBRARY
3 2768 00009305 8